AGU PUBLICATIONS

Geochemistry, Geophysics, Geosystems

RESEARCH ARTICLE
10.1002/2014GC005660

Reconciling subduction dynamics during Tethys closure with large-scale Asian tectonics: Insights from numerical modeling

F.A. Capitanio[1], A. Replumaz[2,3], and N. Riel[1,4]

[1]School of Earth, Atmosphere and Environment, Monash University, Clayton, Victoria, Australia, [2]Institut des Sciences de la Terre, Université de Grenoble Alpes, Grenoble, France, [3]CNRS, Grenoble, France, [4]Now at Department of Earth Sciences, Durham University, Durham, UK

Key Points:
- Coupled subduction and upper plate dynamics modeled
- Break-off drives large-scale rotations, far-field forces drive indentation
- The combinations of these explains the time-dependent Asian tectonics

Correspondence to:
F.A. Capitanio,
fabio.capitanio@monahs.edu

Citation:
Capitanio, F.A., A. Replumaz, and N. Riel (2015), Reconciling subduction dynamics during Tethys closure with large-scale Asian tectonics: Insights from numerical modeling, *Geochem. Geophys. Geosyst.*, *16*, 962–982, doi:10.1002/2014GC005660.

Received 14 NOV 2014
Accepted 27 FEB 2015
Accepted article online 12 MAR 2015
Published online 29 MAR 2015

Abstract We use three-dimensional numerical models to investigate the relation between subduction dynamics and large-scale tectonics of continent interiors. The models show how the balance between forces at the plate margins such as subduction, ridge push, and far-field forces, controls the coupled plate margins and interiors evolution. Removal of part of the slab by lithospheric break-off during subduction destabilizes the convergent margin, forcing migration of the subduction zone, whereas in the upper plate large-scale lateral extrusion, rotations, and back-arc stretching ensue. When external forces are modeled, such as ridge push and far-field forces, indentation increases, with large collisional margin advance and thickening in the upper plate. The balance between margin and external forces leads to similar convergent margin evolutions, whereas major differences occur in the upper plate interiors. Here, three strain regimes are found: large-scale extrusion, extrusion and thickening along the collisional margin, and thickening only, when negligible far-field forces, ridge push, and larger far-field forces, respectively, add to the subduction dynamics. The extrusion tectonics develops a strong asymmetry toward the oceanic margin driven by large-scale subduction, with no need of preexisting heterogeneities in the upper plate. Because the slab break-off perturbation is transient, the ensuing plate tectonics is time-dependent. The modeled deformation and its evolution are remarkably similar to the Cenozoic Asian tectonics, explaining large-scale lithospheric faulting and thickening, and coupling of indentation, extrusion and extension along the Asian convergent margin as a result of large-scale subduction process.

1. Introduction

What drives the deformation in the interiors of continents remain to date mostly unexplained [*Molnar*, 1988]. Continental tectonics during collision must ultimately relate to the subduction zones dynamics, where the fundamental tectonic forces originate. However, the observed complex patterns and evolution of continental tectonics are not easily reconciled with the reconstructed subduction histories, so that the relation between continent margin and interiors processes remains largely unconstrained.

The Asian continent hosts the most spectacular example of continental tectonics. The Cenozoic deformation followed the onset of collision with the Indian plate along its southern margin and propagates over a wide area [*Tapponnier and Molnar*, 1976], with processes ranging from the large-scale faulting and topography build up in Central Asia to the opening of the South China Sea [*England and McKenzie*, 1982; *Tapponnier and Molnar*, 1976; *Tapponnier et al*., 1982].

The causes of the Asian continental tectonics have been a matter of debate for decades and are generally related to two end-member models emphasizing either the role of faulting in the Asian extrusion tectonics [*Peltzer and Tapponnier*, 1988; *Tapponnier et al*., 1982], or the lithospheric viscous (continuous) thickening and flow in the Tibetan Plateau [*England and McKenzie*, 1982; *Houseman and England*, 1993; *Royden et al*., 1997] in accommodating the India-Asia convergence. Although invoking different deformation mechanisms, these models rely on the same assumption that Asian tectonics is the result of the Indian plate northward motion, indenting the continent. Despite widely used, the indenter model is in fact not yet reconciled with the current understanding of the dynamics of plate tectonics, and has not been explained in the context of lithospheric subduction processes [*Mattauer et al*., 1999]. The Asian continent interior deformation during the Cenozoic has been related to the Tethys Ocean closure, subducting along its southern margin

[*Van der Voo et al*., 1999]. During subduction, two main slab break-off episodes have been reconstructed, one at the Ocean-Continent transition between Tethys and India, and one during the resumed Indian continent subduction, while the Indian plate margin was migrating northward [*Guillot et al*., 2003; *Replumaz et al*., 2004; *Replumaz et al*., 2010a]. In this time, the oceanic subduction along the Southeast Asian margin retreated, as shown by tectonic reconstructions and global tomography [*Hall*, 2002; *Replumaz et al*., 2004; *Replumaz and Tapponnier*, 2003].

Subduction provides the driving forces of plate motions and tectonics, so that the evolution of the subducting Tethys must be paired to the Asian plate margin and interior tectonics. Several publications have recently explored the coupling between deformation in continent interiors and subduction processes. Buoyancy perturbations in the subducting lithosphere during oceanic closure, due to varying thermal age or continental lithosphere along the oceanic trench, have the effect of disrupting the trench, forcing relative retreat of less buoyant/oceanic slabs with respect to the buoyant/continental lithosphere [*Bajolet et al*., 2013; *Capitanio*, 2014; *Capitanio et al*., 2011; *Duretz et al*., 2014; *Guillaume et al*., 2013; *Li et al*., 2013; *Magni et al*., 2014; *Sternai et al*., 2014]. Under these conditions, large stresses propagate within continent interiors [*Capitanio et al*., 2011], and back arc-basin opening, thickening and lateral extrusion occur in the coupled upper plate [*Capitanio*, 2014; *Duretz et al*., 2014; *Li et al*., 2013]. Other authors have illustrated how the break-off of the subducting lithosphere alters stress coupling along the margins and widens upper plate deformation, where lithospheric faulting and extrusion occur on the side of back-arc stretching [*Capitanio*, 2014; *Capitanio and Replumaz*, 2013; *Moresi et al*., 2014; *Sternai et al*., 2014]. Others have modeled far-field forcing and subduction processes at the same time coupled with deforming upper plates [*Bajolet et al*., 2013; *Duretz et al*., 2014; *Sternai et al*., 2014]. Almost all of these works have focused on the margin evolution, while the deformation in the plate interior, far from the margin, has been relatively less illustrated.

Here, we focus on the coupling of subduction and upper plate deformation to elucidate the controls of long-term Tethys oceanic closure and Indian continent subduction on the Asian continent interiors tectonics by means of three-dimensional numerical modeling. Our modeling approach aims to meld previous studies that have either addressed the intraplate lithospheric deformation under imposed boundary motions or studied the processes at the convergent margin. We systematically model perturbations to slab buoyancy force driving subduction and convergence, due to continental lithosphere entrainment and slab break-off, and external forcing, such as ridge push and far-field forces, to explore their influence on the tectonics of the upper plate interior. Then, we draw inferences on the coupled Cenozoic evolution of the Indian and Southeast Asian subducting margins and the large-scale Asian tectonics.

2. Numerical Modeling

2.1. Modeling Approach

We use a three-dimensional numerical model embedding the downgoing and upper lithospheric plates and the ambient fluid. This setup allows capturing the force balance during lithosphere subduction and its interactions with upper lithosphere and the study of the coupling of slab buoyancy, ridge push, and far-field forces with the upper plate margin and interiors deformation.

The model setup is designed to reproduce geological and modeling constraints of the investigated area. We thus focus on the Asian plate, allowing for a fixed boundary in the west and a stress-free boundary on the north and east [e.g., *England and Houseman*, 1985; *Tapponnier et al*., 1982] and add a Tethys plate, embedding a continental Indian plate bordered by mid-oceanic ridges on the east and south and by a transform margin on the west of India [e.g., *Zahirovic et al*., 2012].

Different modeling efforts have emphasized the role of rheology in the Asian tectonics, which range from viscous thickening of the crust/lithosphere, to crustal flow and large-scale faulting/shearing. Here, we use a composite viscoplastic rheology which encompasses the diverse deformation regimes, viscous flow at low stresses and plastic faulting/shearing at larger stresses.

We adopt several simplifications in order to reduce the number of free parameters. While enabling us to better constrain the parameters' contribution, this provides a first-order understanding of the processes involved. We focus here on plastic deformation, thus we do not address the nonlinear temperature and stress dependences of viscous rheology, and chose instead a Newtonian, temperature-independent

viscosity. The linearization likely affects the magnitude of viscous deformation, i.e., strain rates [*England et al*., 1985], although does not affect the deformation mode, viscous flow or yielding, which depends on the threshold stress. The upper plate has no density contrast with the mantle and free-slip boundary condition on the model's top, that is no free-surface. This choice prevents topography, yet allows for thickening of the plate [e.g., *Cook and Royden*, 2008; *England and Houseman*, 1985; *England and McKenzie*, 1982]. Although embedded in our models, we do not address dynamic topography, that is the component due to mantle tractions: the models' transient behavior and strong horizontal deformation gradients at the surface would yield no reliable dynamic topography assessment [*Gurnis et al*., 1997]. Therefore, our study is to be regarded as complimentary to those studies focused on the role of topography [*Clark*, 2012; *Copley et al*., 2010; *Iaffaldano et al*., 2011] and the strain field in Asia [*Flesch et al*., 2001; *Ghosh and Holt*, 2012; *Ghosh et al*., 2006].

Another relevant modeling simplification is related to the far-field forces. It is accepted that ridge push and far-field forces had a relevant impact on Cenozoic Indian motions [*Becker and Faccenna*, 2011; *Cande and Stegman*, 2011; *Capitanio et al*., 2010a; *van Hinsbergen et al*., 2011b]. Therefore, we test the role these might have on the convergent margin-upper plate coupling, rather than their different mechanisms, imposing velocity boundary conditions to the downgoing plate. A shortcoming of this approach consists in constrained downgoing plate motions, and thus these will not be addressed here. More realistically, plate motion estimates are rather sensitive to the global net torque around plates and large-scale mantle circulation [*Becker and O'Connell*, 2001; *Conrad and Lithgow-Bertelloni*, 2002], so that using the detailed Indian motions would provide nonunique constrains. Instead, we focus on the stresses at the convergent zones, which are less constrained by subduction zones motions, i.e., frame-independent [*Capitanio et al*., 2010b; *Goes et al*., 2011].

2.2. Governing Equations

Subduction is modeled as the incompressible, viscous flow of an infinite Prandtl number fluid at very low Reynolds number. Under these approximations, the force balance is governed by the conservation of mass, enforcing the incompressibility condition, and momentum equations:

$$\nabla \cdot \mathbf{u} = 0 \tag{1}$$

$$\nabla \cdot \sigma = \mathbf{f} \tag{2}$$

where $\mathbf{u}$ is the velocity vector, σ the stress tensor, and $\mathbf{f} = \rho\mathbf{g}$ the force term, with ρ the density and $\mathbf{g}$ the gravity vector. The stress tensor splits into a deviatoric part, τ, and an isotropic pressure p:

$$\sigma = \tau - p\mathrm{I} \tag{3}$$

where I is the identity tensor and p is the pressure. The constitutive equation relating the stresses with the velocity gradients is given by the generalized Newtonian model of the form:

$$\tau = 2\eta\dot{\varepsilon}, \tag{4}$$

where η is the dynamic viscosity and $\dot{\varepsilon}$ is the strain rate tensor:

$$\dot{\varepsilon}_{ij} = \frac{1}{2}\left(\frac{\partial u_i}{\partial x_j} + \frac{\partial u_j}{\partial x_i}\right) \tag{5}$$

Plasticity is implemented defining a depth-dependent yield stress:

$$\tau_Y = C_0 + C_1 z \tag{6}$$

where C_0 is the cohesion at zero confining pressure, C_1 is the depth-dependent coefficient, and z is the depth. We then implement the composite viscoplastic flow law through the definition of the effective viscosity:

$$\eta^{eff} = \min\left(\eta, \frac{\tau_Y}{2\dot{\varepsilon}_{II}}\right) \tag{7}$$

where $\dot{\varepsilon}_{II} = \sqrt{\dot{\varepsilon}_{ij}\dot{\varepsilon}_{ij}/2}$ is the square root of the second invariant of the strain rate tensor. equation (7) enforces the plasticity criterion $\tau = \tau_Y$ for $\tau > \tau_Y$.

Table 1. Model Parameters Used in the Experiments

Quantity	Symbol	Value
Gravitational acceleration	**g**	9.81 m s^{-2}
Models size	x × y × z	5000 × 4000 ×1000 km
Mantle		
Upper mantle thickness		660 km
Upper mantle viscosity	$\eta 0$	2.5×10^{20} Pa s
Upper mantle density	$\rho 0$	3300 kg m^3
Lower mantle thickness		340 km
Lower mantle viscosity		2.5×10^{21} Pa s
Subducting plate		
Initial length		2250 km
Width		2700 km
Plastic crust thickness		30 km
Cohesion	C_0	20 MPa
Friction coefficient	μ	0.6
OCB Friction coefficient	μ	0
Oc. lithos. density contrast	$\Delta\rho_O$	75.7 kg m^{-3}
Cont. lithos. density contrast	$\Delta\rho_C$	[12.6, 25.2, 50.4] kg m^{-3}
Continental plate width		1000 km
Continental plate length		2000 km
Upper plate		
Width		3000 km
Length		2450 km
Thickness		50 km
Density contrast		0 kg m^{-3}
Viscosity		2.5×10^{23} Pa s
Cohesion	C_0	45 MPa
Friction	M	0

Equations (1) and (2) are solved in their nondimensionalized form using a Particle-in-cell finite element method, Underworld [*Moresi et al.*, 2003]. This method uses Lagrangian particles embedded in the Eulerian finite-element mesh, where the material properties and their interfaces are stored, allowing accurate tracking of history-dependent material properties such as stress and strain, and minimizing the numerical diffusion. The details of the numerical method, software implementation, and relevant numerical benchmarks are described in *Moresi et al.* [2003].

2.3. Model Parameters and Setup

The subduction system model setup includes the downgoing and upper plate immersed in the mantle. The model space is a 3-D Cartesian box 5000 × 4000 × 1000 km in the directions *x*, *y*, and *z*, respectively (Table 1), with a numerical resolution of 384 × 192 × 64 elements and 94,371,840 Lagrangian particles (Figure 1a). The model's boundary conditions are free-slip on top and sidewalls, no-slip on the bottom, and periodic boundary conditions in the front and rear walls, i.e., in the subduction direction, to reduce the constraining wall effect (Figure 1b). Resolution tests of the models and this setup have been published by *Schellart and Moresi* [2013], and *Stegman et al.* [2006].

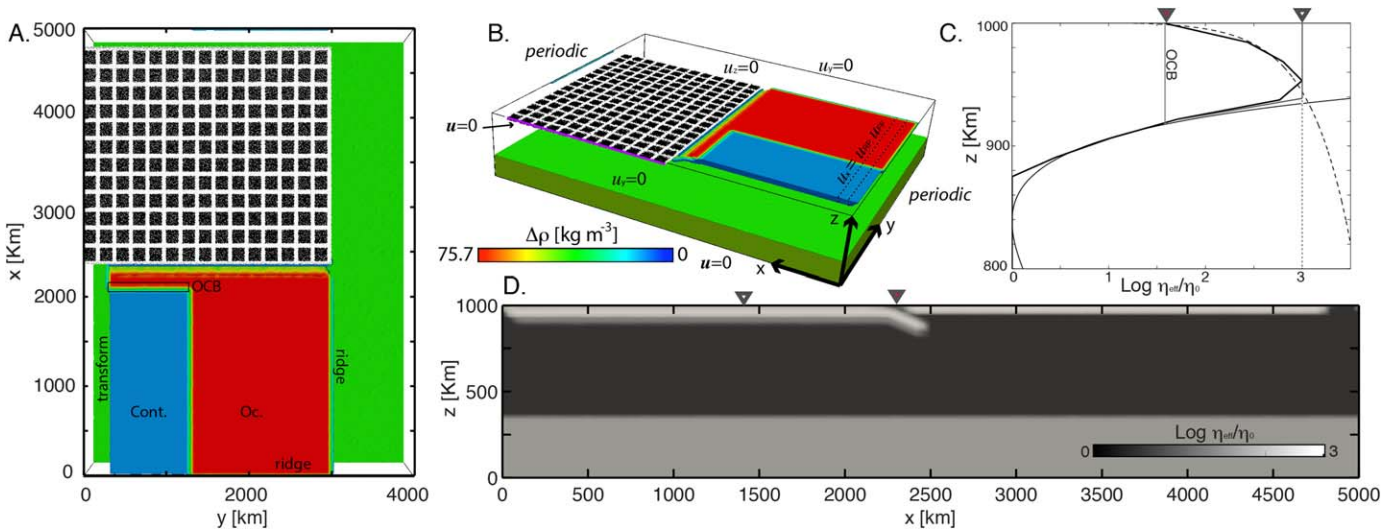

Figure 1. Numerical model setup. (a) Top view of the model space, contour of the viscosity field $\eta_{eff}/\eta_0 = 100$, color scale for density contrast with the mantle, with Continental (Cont.) and Oceanic (Oc.) lithosphere. Ocean-continent boundary (OCB) is indicated by the black thin line. Lagrangian particles shown for the upper plate only, colored for reference. (b) Boundary conditions of the model. Dashed lines for the volume where velocity boundary conditions u_x = const are applied (Model B and C, only). (c) Viscosity profiles of the models' upper 200 km. Thick black line for the oceanic lithosphere at the plate margin, i.e., under large stresses (location in Figure 1d, red triangle), thin black line for oceanic lithosphere profile (location in Figure 1d, white triangle). OCB indicates the profile at the ocean continent boundary. Thin black curve for effective viscosity after [*Karato and Wu*, 1993] $\eta_{eff} = A^{-1/n}\dot{\varepsilon}_0^{(1-n)/n} exp[(E_a + PV_a)/nRT]$, where the prefactor *A*, reference strain rate $\dot{\varepsilon}_0$, exponent *n*, activation energy, and volume E_a and V_a, are for dry Olivine, and *P* and *T* are taken for a half-space cooling model for an oceanic plate of 80 Ma [*Turcotte and Schubert*, 1982]. Dashed vertical curve for the effective viscosity under the plastic regime in equation (6). Dotted line is the viscosity limiter. (d) Cross section of the viscosity field (y = 2000 km). The triangles indicates the profile locations in Figure 1c.

The viscosity profile of the downgoing lithosphere is implemented to reproduce the laboratory constraints on Olivine [*Karato and Wu*, 1993] (Figure 1c). Using the parameters of dry Olivine, a minimum viscosity of $\eta_0 = 2.5 \times 10^{20}$ Pa s in the sublithospheric mantle (see figure caption) is predicted, which we use here as the reference viscosity. This value is imposed constant in the mantle throughout the upper 660 km, with an increase of a factor 10 in the lower mantle (Figure 1d). These values are in agreement with average effective viscosities of 5.3×10^{20} Pa s and 2.3×10^{21} Pa s, for the upper and lower mantle, respectively [*Paulson et al*., 2007]. The subducting lithosphere's strength is limited by the plastic law in equation (6), with $C_0 = 20$ MPa, $C_1 = \mu\rho_0$ **g**, where $\mu = 0.6$ the friction coefficient, and $\rho_0 = 3300$ kg m^{-3} the reference density. Elsewhere in the oceanic plate model maximum viscosities are limited to $10^3 \times \eta_0$ (Figures 1c and 1d, white triangle).

The density of the oceanic lithosphere is scaled to match the values of oceanic slab buoyancies. Estimated Earth-like subducting slab buoyancy of $F_B = 4.9 \times 10^{13}$ N m^{-1} is inferred when the elevation of the Olivine-Spinel transition is included [*Turcotte and Schubert*, 1982]. For the model lithosphere of thickness $h = 100$ km and length $l = 660$ km, the scaled reference density contrast for oceanic lithosphere is $\Delta\rho_0 = F_B/\mathbf{g}hl = 75.7$ kg m^{-3} (Figures 1a and 1b). Continental lithosphere densities can vary largely, from -100 kg m^{-3} to values of 45 kg m^{-3} [*Cloos*, 1993]. Modeling constraints and recovered thicknesses of the crustal unit in the Zanskar Ranges [*Capitanio et al*., 2010a] yield a depth-averaged Greater Indian lithosphere density contrast of $\Delta\rho = 12$ kg m^{-3}. Here we have tested values of $\Delta\rho_C = 12.6$, 25.2 and 50.4 kg m^{-3}.

The different density domains are embedded into the downgoing plate. The subducting plate embeds a lithosphere of density contrast $\Delta\rho_0$, henceforth the oceanic lithosphere, and one of density contrast $\Delta\rho_C$, henceforth called the continental lithosphere (Figure 1a). The oceanic lithosphere is 2700 km wide and 2250 km long, and the continental lithosphere is 1000 km wide and 2000 km long. We have shaped the right and bottom (in plan view, Figure 1a) margins of the downgoing plate as mid-oceanic ridges, that is tapering out in the last ~100 km, whereas on the left the margin is vertical, mimicking the transform fault reconstructed along this obliterated margin [e.g., *Zahirovic et al*., 2012]. Due to uncertainties in the reconstructions, we have also tested a ridge margin on the left, although the results for the continental tectonics are the same. While the periodic boundary conditions allow for unconstrained mantle flow in the convergence direction, the toroidal component of the flow might be restrained by the sidewalls [e.g., *Funiciello et al*., 2004]. Nonnegligible toroidal flow does not extend more than ~300 km from the slab edge [*Jadamec and Billen*, 2010], so that the distance of 1000 and 350 km from the edge have a minor impact on the subducting slabs. Furthermore, constrained toroidal flow does not affect the sinking [*Bercovici*, 1995], i.e., the buoyancy forces, which are the focus of this work. We have investigated several configurations, allowing for larger space around plates, the surface tectonics outcomes were not affected. The sidewalls configurations also follows the tomographic constraints, showing that the Tethys slab was likely isolated to the east and separated, yet rather close, to the slab beneath Zagros, during its evolution [*Hafkenscheid et al*., 2006], although this is not addressed here.

The convergent margin between plates is implemented here in an implicit way. In other numerical models, the plate interface has been implemented by either prescribing slip conditions along the interface fault [*Zhong and Gurnis*, 1995] or prescribing a low-viscosity zone allowing for low shearing stresses [e.g., *Billen and Hirt*, 2005; *van Hunen and Allen*, 2011]. Here, it is implemented through a viscoplastic flaw law applied to the first 30 km [*Capitanio et al*., 2011; *Capitanio et al*., 2010b], where the plastic failure stresses are lower than creeping stresses [*Kohlstedt et al*., 1995]. The lower cohesion of this layer provides the weak layer required for single-sided, sustained subduction [*Crameri et al*., 2012]. This type of implementation enables stress coupling across the subduction zone itself and allows consistent trench motions [*Capitanio et al*., 2010b, 2011]. In the initial configuration, the downgoing plate extends in the mantle to 150 km depth. The subsequent subduction evolution is self-sustaining owing to the buoyancy of the developing slab.

The subduction of Ocean-Continent Boundary (OCB) is associated with large tensile stresses leading to break-off. While we refer the reader to some more focused work on the thermomechanical modeling of such process [*Burkett and Billen*, 2010; *Duretz et al*., 2012; *Gerya et al*., 2004; *van Hunen and Allen*, 2011], here we focus instead on the implications of slab break-off for continental tectonics, and differentiate the rheology at the OCB to constrain the development of break-off. The OCB is a 100 km wide belt in front of the subducting continent with the same rheology as the oceanic lithosphere (Figure 1a), yet we suppressed the

depth dependence in equation (6), i.e., $C_1 = 0$, thus leading to an OCB of strength ~40% smaller than the surrounding lithosphere (Figure 1c, gray line).

Inversion of geodetic, geologic, topographic, and seismic data constrain the depth-averaged viscosity of the Asian lithosphere to $\sim 10^{21}$ Pa s and $\geq 10^{23}$ Pa s, for deforming and rigid areas, respectively [*England and Molnar*, 1997; *Flesch et al*., 2001]. We constrain the viscosity of our upper plate model to these values, constant in depth. This is done in the models setting $C_0 = 45$ MPa and $C_1 = 0$ in (6) resulting in a model viscosity, constant with depth, of $\sim 10^{21}$ Pa s in plastically deforming areas, and to 2.5×10^{23} Pa s elsewhere, yielding viscosity contrasts with the mantle of 10–100 times, in agreement with the estimated Asian continent values [*England and Molnar*, 1997]. The plastic strength of the continental lithosphere reduces to the integrated yield stress over the thickness of 50 km, that is 2.25×10^{12} N m^{-1}. This values compares to the low estimates of continental lithospheres' integrated strength of $10^{12}-10^{13}$ N m^{-1} [*Burov*, 2007], and compatible with the suggestions that the lower crust might be weak or might contain melt, whereas most of the lithospheric strength remains confined in its upper portion [*Flesch et al*., 2001].

The upper plate is 3000 km wide and 2450 km long, and extends laterally above the whole subduction zone. It has the left margin attached to the model space wall, where it is fixed, i.e., $\mathbf{u} = 0$ (Figure 1b, purple line). In order to isolate the behavior of the upper plate under tectonic forcing, the upper plate has no buoyancy, i.e., no density contrast with the mantle. Therefore, no lithostatic pressure develops along the margins immersed in the mantle, and deformation occurs only under stresses propagated from the convergent margin.

2.4. Ridge Push and Far-Field Forcing

Other than the forces arising from the subduction of lithosphere, we test in two suites of models the role of ridge push and far-field forcing. GPE analyses and modeling have suggested that the gravitational potential of the mid-oceanic ridge, the ridge push, sustains the topographic load of Tibet [*Ghosh and Holt*, 2012; *Ghosh et al*., 2006; *Molnar and Lyon-Caen*, 1988]. In a dynamic model, a tangential force of the order of the ridge push is required to explain the large indentation of the Indian margin overriding its deeper slab since ~40 Ma [*Capitanio et al*., 2010a]. In the models here we impose a trenchward, i.e., *x*-parallel, velocity to the downgoing plate equal to that measured along the oceanic subduction $u_{RP} = 2.5$ cm yr^{-1}. That is, we measure the downgoing plate velocity in the free, slab buoyancy driven models and we constrain the subducting plate velocity in this suite of models to be equal. This is applied as an internal boundary condition to the volume 100 km long, as wide as the whole downgoing plate, at the rear of the plate margin (Figure 1b, dashed line), extending at depth throughout the downgoing plate thickness. This internal boundary condition results in a trenchward force within the lithosphere, similar to the ridge push, otherwise not present in the slab buoyancy-only driven models. Henceforth, we refer to this boundary condition's effect as the ridge push force F_{RP}.

To explain the Cenozoic fast Indian motions, far-field forces have been invoked. The causes for these forces might relate to stress propagation from neighboring south-east Asian subduction [*Li et al*., 2008], transient plume head push [*Cande and Stegman*, 2011; *van Hinsbergen et al*., 2011b], or also large-scale flow [*Becker and Faccenna*, 2011] linked to the deeper sinking of the Tethys slab in the lower mantle [*Becker and Faccenna*, 2011; *Capitanio et al*., 2010a]. While constraining the magnitude of this force is out of the scope of this paper, we assume that far-field forces must be in the same order of net slab pull and ridge push forces on Earth, and they add linearly to the force balance of the single subduction zone. These considerations are compatible with the outcomes of GPE analysis [*Ghosh et al*., 2006] suggesting that Tibetan topography potential is balanced by forces ~2.5 times higher than that of the Indian Mid Oceanic Ridge. We then simplify the internal boundary conditions to an imposed plate trail velocity $u_F = 2\, u_{RP} = 5$ cm yr^{-1}. In the remainder of the paper, the force following this boundary condition is referred to as far-field forcing F_F.

2.5. Deformation Analysis

To illustrate the models strain field, we use the second invariant of the strain rate tensor as defined in the previous section, the compressive and extensional strain rate axes and the vertical strain rate. The eigenvectors of $\dot{\varepsilon}$ are the principal axes of the strain rate ellipsoid of values λ_1 the maximum, λ_2 the intermediated, and λ_3 the minimum. Surface rate of strain axes are defined using the largest and smallest eigenvectors of the tensor $\dot{\varepsilon}$. Where $\lambda_i >> \lambda_j$, with $i, j = 1, 3$ and $i \neq j$, the volume is under uniaxial strain. Uniaxial extension

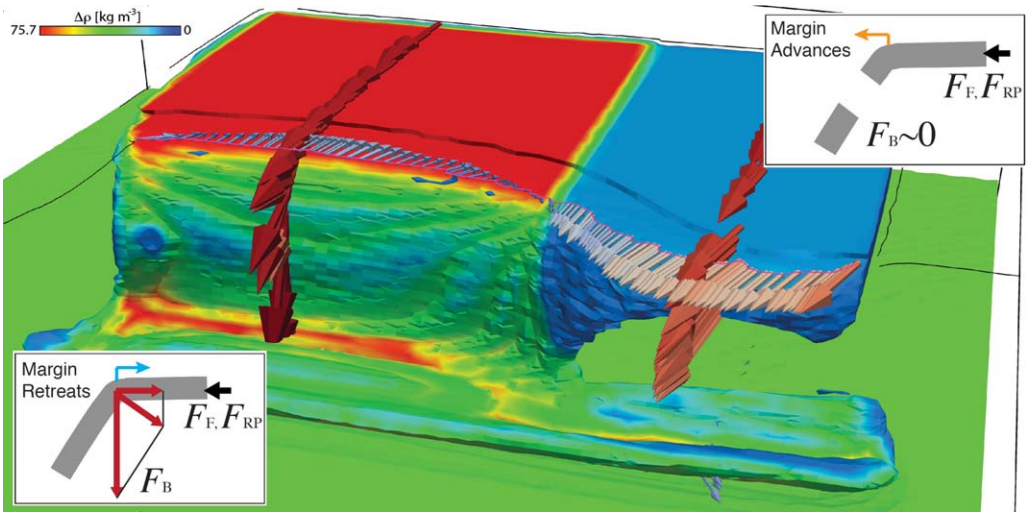

Figure 2. Sketch of the force balance around subducting plates and resulting margin motions. Contour of the viscosity field as in figure 1, model B is shown (Figure 3b). The large red arrow in the center of the continental (blue) and oceanic (red) lithosphere indicate the plate velocity. Thin blue-orange-red arrows for the trench motions. In the bottom left inset, sketch of the oceanic margin force balance and motions, slab buoyancy vertical force (F_B) projects to the horizontal resulting in rearward force. This latter overcomes the ridge push and far-field force (F_{RP}, F_F), therefore the convergent margin retreats. In the top right inset, the sketch for the continental margin where slab break-off occurs. Here, same ridge push and far-field force apply, yet, because the slab buoyancy F_B vanishes, margin advances.

occurs when $\lambda_1 >> \lambda_3$, and compression when the opposite is true. When $\lambda_1 \approx \lambda_3$ the deformation regime is plane strain and minor or no thickness variation occurs, as in the case of strike-slip motions.

The rate of change of plate thickness is indicated by the vertical strain rate measured on the top boundary. From the incompressibility condition (1) follows that:

$$\dot{\varepsilon}_{zz} = -(\dot{\varepsilon}_{xx} + \dot{\varepsilon}_{yy}), \tag{8}$$

thus positive values of (10) indicate an excess of compression compensated by vertical thickening, instead negative values of (10) show that vertical thinning compensates the extension in the horizontal plane, whereas no thickness variations occurs for $\dot{\varepsilon}_{zz} = 0$.

Because the plasticity flow law implemented introduces a nonlinear relation between stress and strain rate, these patterns can be largely different, with strong localization in the latter. Therefore, besides the strain rates, we illustrate the stress coupling using the magnitude of the component of the stress tensor τ_{xx}, that is in the direction parallel to the convergence. Since the downgoing plate velocity is positive, $\tau_{xx} < 0$ in the upper plate indicates compression, that is trenchward stresses arising from the compression, the opposite is true when $\tau_{xx} < 0$, then the upper plate is under tension.

Finally, to assess the finite strain in the models, we have added a reference grid in the Lagrangian particles of the model's upper plate, with 50 km wide bands separating 150 km wide squares (Figure 1a). Because the material particles are advected, the grid illustrates the finite strain.

3. Results

A suite of numerical models was carried out varying the buoyancy contrast of the continental plate and the boundary conditions to the subducting plate. We group the models in three classes: Model A, only driven by subduction force, Model B, including subduction force and ridge push, and Model C, including subduction and far-field forces. The results are presented in two sections: the first presents the controls of the force balance on the subduction zone evolution, the second the controls on the upper plate interiors tectonics.

3.1. Controls on Convergent Margin Migrations

For the three models, during the initial stage, the progressive sinking of the oceanic lithosphere in the mantle develops into a subduction zone along the convergent margin, driving plate convergence. In this stage, the margin is stable, and deformation is mostly accommodated at the trench. As the heterogeneous plate

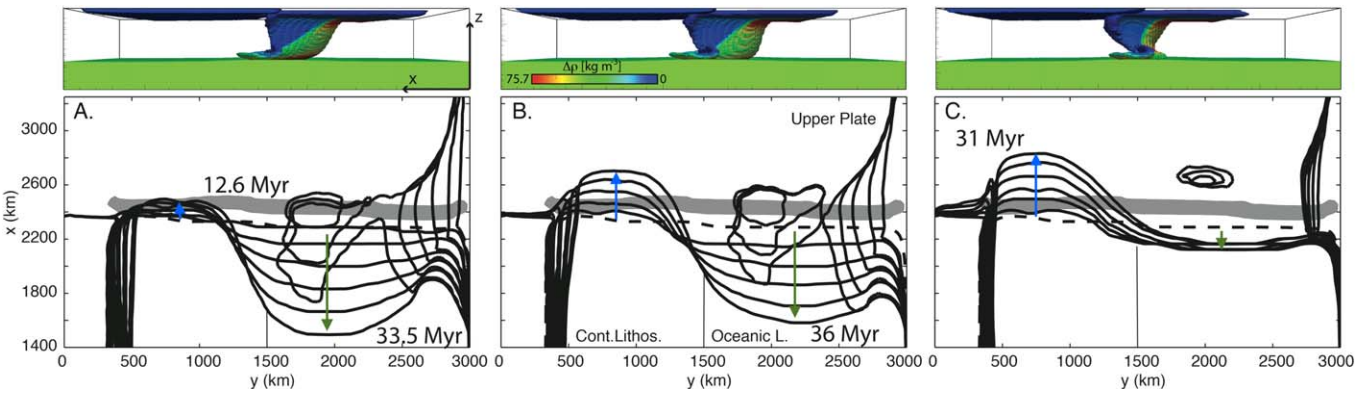

Figure 3. (top) Models at the final stage and (bottom) margin migrations synthesis. (top) Contour of the viscosity field as in Figure 1. The age of the final stage is reported in the bottom plots. (bottom) Contour of the top surface viscosity (black line) indicating the plate margins and the back arc basin opening. Dashed line for the convergent margin's position at time of break-off, 12.6 Myr. Gray-filled contour for the final position of the detached slab, cross section at 500 km depth. Models shown are Model A, that is slab buoyancy-only driven (no external forcing), Model B, slab buoyancy driven and ridge push and Model C, slab buoyancy driven and far-field forces. Green arrows indicate margin retreating motions in time, in blue advancing margin motions in time.

(hosting oceanic and continental lithosphere) is entrained in the trench, continent subduction onsets and a collisional margin forms. The density change associated with the OCB results in stresses in the lithosphere past the yield strength, resulting in the detachment of the deep portion of the oceanic slab from the continental lithosphere. This occurs at shallow depths of ∼150 km, 12.6 Myr since the model starts.

Continent subduction and slab break-off perturb the subduction forces leading to differential margin motions (Figure 3). We present three models here to illustrate that the convergent margin migrations are best understood in the context of the balance of the driving subduction forces along the margin and external forces, propagated through to the downgoing plate (Figure 2). In the model A, subduction only drives convergence; the net force at the margin is only the net slab buoyancy F_B. Upon subduction of heterogeneous plate, the buoyancy pull force along the oceanic margin has not varied, yet it vanishes along the collisional margin, where the slab detaches. While subduction vanishes in this latter portion of the trench, sinking of the oceanic plate is accommodated by margin retreat. Different margin motions result in trench curvature increasing with time (Figure 3a). The mantle drag and toroidal flow around the oceanic slab edge force curvature during retreat [e.g., *Morra et al.*, 2006], whereas part of the continental lithosphere is dragged into the mantle on the opposite side. While the total oceanic margin retreat is 800 km (green arrow), indentation along the collisional margin is negligible, as this mostly remains aligned with the original position at the time of break-off (dashed line) and the deep position of the sunken oceanic slab (gray-filled contour).

In model B, forced convergence drives indentation along the collisional margin, whereas it has a negligible effect on the oceanic margin motions (Figure 3b). The collisional margin advances toward the upper plate (blue arrow), and overrides the deeper detached slab by ∼400 km, which has now reached the transition zone depth (gray-filled contour).

In the model C, far-field forcing additionally drives convergence, the net oceanic trench motions vanish, and the oceanic margin becomes eventually stationary (Figure 3c). This balance is achieved rapidly, although allows a total retreat of <200 km (green arrow). Similarly to the previous case, the continental collision margin advances (blue arrow), overriding by ∼470 km the deeper slab (gray contour).

Summing up (Figure 3), slab buoyancy gradients alone result in minor indentation along the collisional margin and retreat along the oceanic trench (Model A). Far-field forces always result in larger indentation along the stalled margin, where the slab had broken off, and migration of the subduction zone to override its deeper slab. Along the oceanic subducting margin, ridge push does not hamper oceanic trench retreat (Model B), and when far-field forcing is large enough to fully balance the slab retreat, the margin remains rather stationary (Model C).

3.2. Controls on Coupled Margin: Plate Interiors Tectonics

3.2.1. Stress and Velocity Fields

The break-off of the subducting slab results in coupled margin-plate interiors deformation, due to the increased stress coupling across the margin, followed by rotations, and shearing in the upper plate interiors.

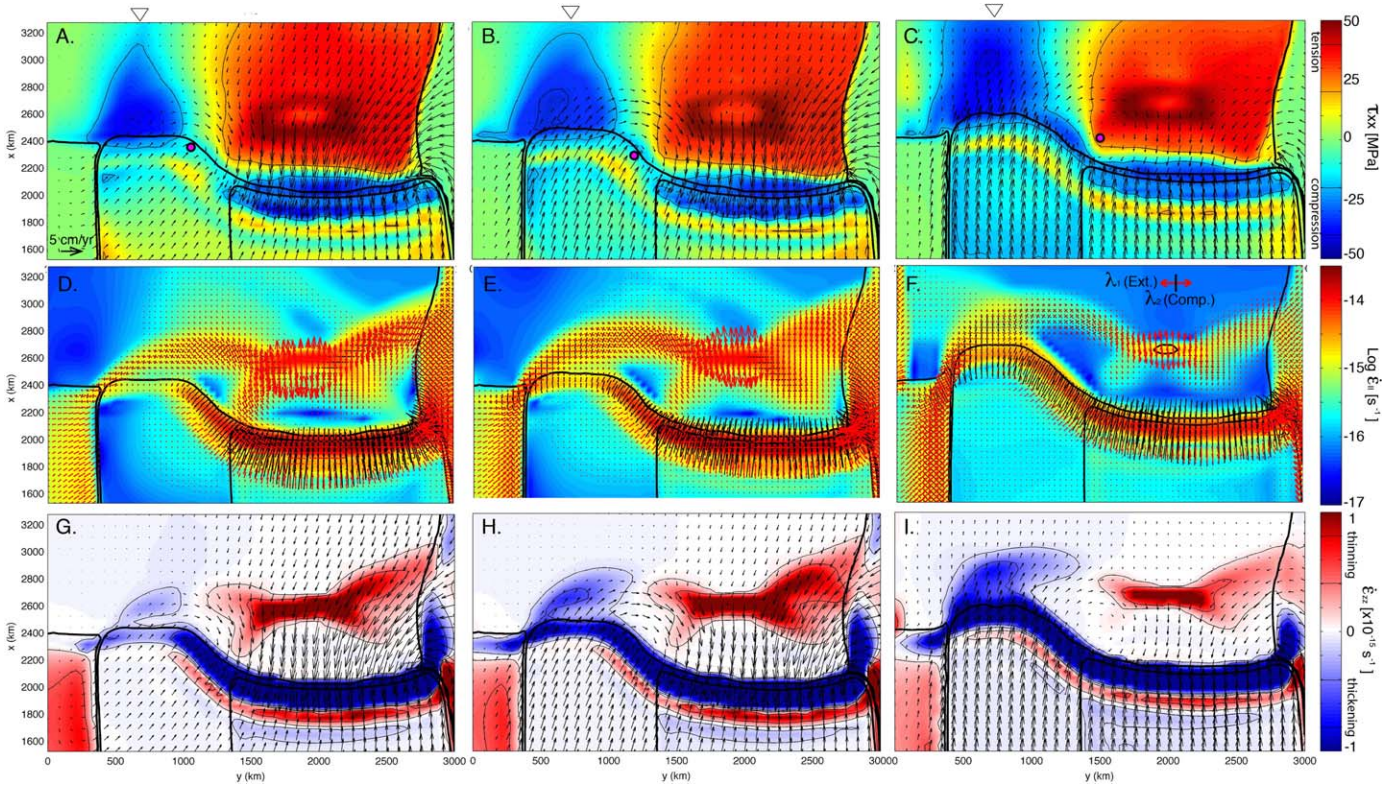

Figure 4. Surface stress, velocity, second invariant of the strain rate, and vertical strain rates for the models in Figure 3. The models are shown at ~19 Myr, ~7 Myr after break-off. Black contour lines for viscosity contrasts $\eta_{eff}/\eta_0 = 10$, and for density contrast of 70 kg m^{-3}, indicating the oceanic lithosphere in the downgoing plate. Deviatoric stress component τ_{xx} in the *x* direction and velocity vectors in Models A (a), B (b), and C (c), $\tau_{xx} > 0$ is for extension, $\tau_{xx} < 0$ for compression. Purple circle indicates the approximate rotation pole in the upper plate clockwise rotations. Second invariant of the strain rate tensor $\dot{\varepsilon}_{II}$ and horizontal strain rate ellipsoid axes, largest and minimum, for Models A (d), B (e), and C (f), black bars for compression and red arrows for extension. The largest axis is scaled with the magnitude of the second invariant. Vertical strain rates $\dot{\varepsilon}_{zz}$ and velocity vectors for Models A (g), B (h), and C (I). In the top plate, vertical strain rates indicates plate thinning (red) and thickening (blue), although in the subducting plate this is mostly instead associated with the downwelling during subduction and flexure, and is to be disregarded. Triangle above in Figures 4 a–4c indicate the location of the profiles in Figures 6 and 7.

Along the oceanic margin, viscous coupling between the slab, mantle, and the upper plate results in the localization of deformation in a back-arc basin, and convergence-parallel tension of ~45 MPa, mostly localized ~550 km from the trench (Figure 4). The return flow associated with the sinking slab causes tractions beneath the upper plate, forcing tensile stresses in the upper plate, where the flow is divergent, and compressional stresses where the flow converges, at the plate margin (Figure 5b), here shown for Model B. The stress regime in the upper plate varies rapidly from compressive, along the margin, to tensile at 125 km (Figure 5a). The stresses around the convergent margin, to a distance of ~550 km from the trench, are constant around the same values and independent of the increasing far-field forces (Figures 4a, 4b, and 4c). In fact, the forced convergence cannot speed up the vertical sinking of the slab, so that the horizontal forcing to the convergence is accommodated by larger downgoing plate velocity and trench motions, instead of increased slab sinking. Because the buoyancy-driven vertical motions of the slab and mantle flow do not change when far-field forces apply, the stresses in the upper plate are consequently constant.

Along the continental margin, during the continental subduction phase, the trench-perpendicular stress component in the upper plate is negative (compression) close to the margin, positive (tension) in the upper plate interiors close to the trench, and negative at larger distance, mostly due to the large-scale deformation of the plate (Figure 6). During slab break-off the convergence is accommodated at shallow depth along the collisional margin (Figure 5c, shown for Model B), propagating large stresses across, as large as ~35 MPa in the 100 km from the margin. Stress decays with distance from the trench, although the whole upper plate remains under moderate compression. The compressional stress pattern above the stalled margin attains a triangular shape, which under the effect of far-field forces extends further in the plate interior (Figures 4a, 4b, and 4c).

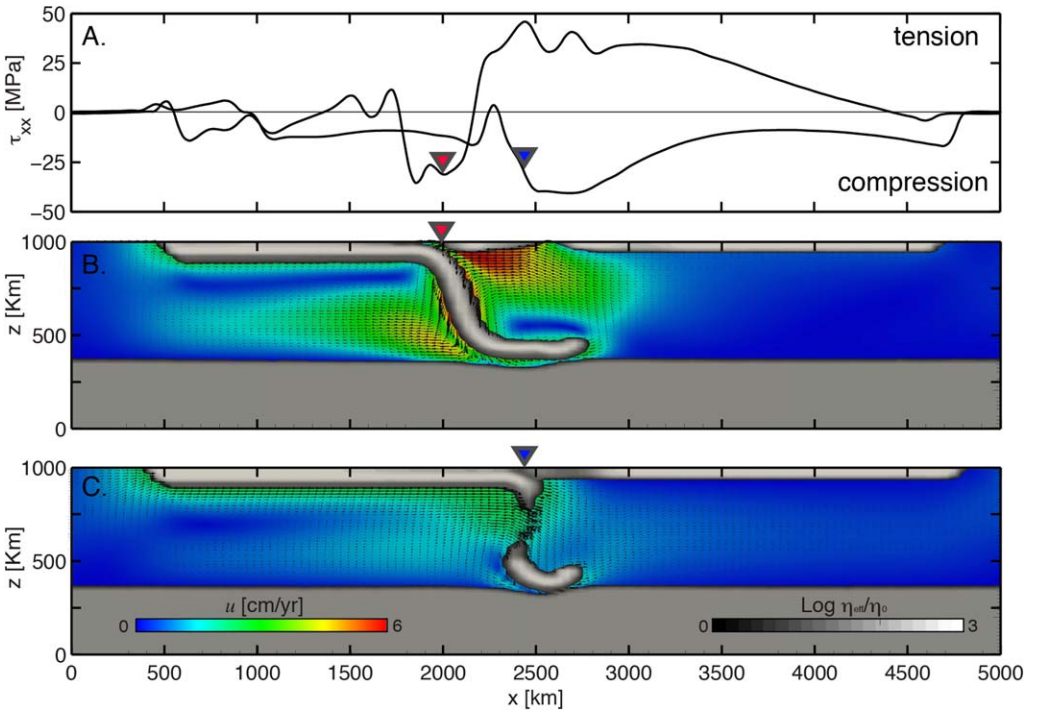

Figure 5. Surface stresses profiles and viscosity mantle flow section for the Model B in Figure 4. (a) Deviatoric stress component τ_{xx} at $y = 750$ (blue triangle) km and $y = 2000$ km (red triangle). (b) Cross section of the viscosity and mantle flow along the center of the oceanic subduction zone at $y = 2000$ km and (c) cross section of the viscosity and mantle flow along the center of the continental subduction zone at $y = 750$. The triangles indicate the location of the plate margin-subduction trench. The velocity magnitude (color-coded) is illustrated for the mantle ($\eta_{eff}/\eta_0 < 10$), for larger values (gray color-scale) we show the viscosity contrast.

The upper plate velocity pattern shows the migration following the oceanic margin retreat, yet away-from-trench motions with a lateral component occur along the collisional margin (Figure 4a). The upper plate large motions are limited to a triangular area in front of the indenter, bounded by a narrow belt, departing at ~45° from the trench, where the shear is maximized. The motions of the block in between indicate extrusion. The extruding block undergoes extension, localized along a trench-perpendicular belt approximately located above the ocean-continent margin, although here this is considered a second order feature. We find an upper plate rotational axis located close to the trench (purple circle). The internal deformation during rotations, i.e., nonrigid body motions, prevents the definition of a rotation axis, so that the rotation axis is here approximated by the maximum in the velocity field's curl. The location of the rotation pole does not migrate largely during the evolution. Under the effect of the ridge push force (Model B), the indentation,

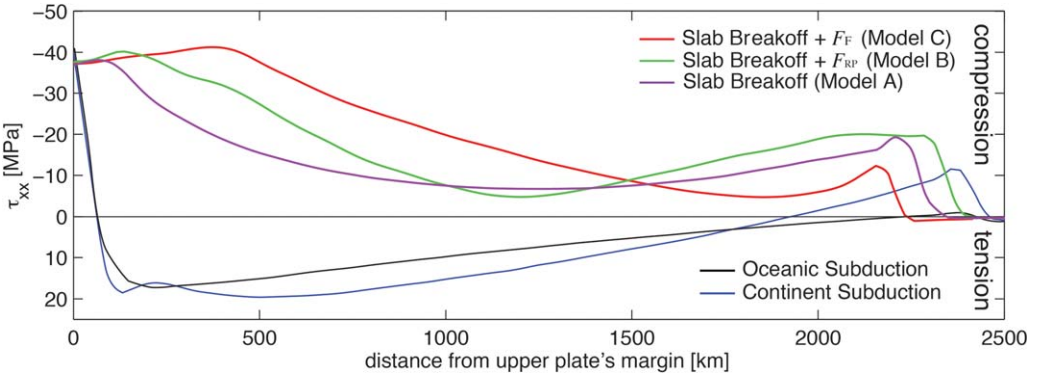

Figure 6. Deviatoric stress component τ_{xx} profiles during different phases and models in the upper plate above the continental subduction ($y = 750$ km), versus the distance from the plate margin/subduction trench. The oceanic and continental subduction profiles (black and blue lines) refer to the model where no boundary conditions are imposed, before break-off. The cross sections for Models A, B, and C are taken from Figure 4.

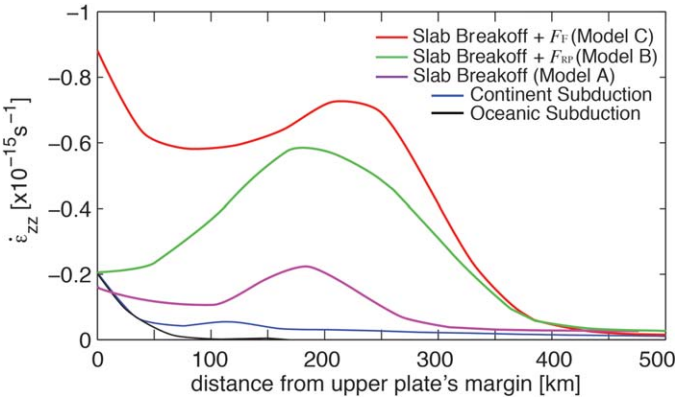

Figure 7. Vertical strain rate $\dot{\varepsilon}_{zz}$ profiles during different phases and models in the upper plate above the continental subduction ($y = 750$ km, location in Fig. 4) versus the distance from the plate margin/subduction trench. The oceanic and continental subduction profiles (black and blue lines) refer to the model where no boundary conditions are imposed, before break-off. The cross sections for Models A, B, and C are taken from Figure 4.

i.e., the trench perpendicular velocity component, increases, while the lateral extrusion component, driven by the oceanic margin retreat, remains almost unvaried (Figure 4b). The rotation pole of the extrusion motions remains located close to the margin, along the downgoing plate. Under the effect of far-field forces (Model C), the indentation motions further increase, but hamper the oceanic trench retreat (Figure 4c), while the extruding block's rotation pole progressively shifts toward the upper plate (purple circle).

The choice of the velocity boundary conditions limits the motions of the downgoing plate. Model A and Model B have the same convergence velocity along the oceanic subducting margin, and the downgoing continental lithosphere is mostly affected by the imposed convergence. Because the applied velocity is only prescribed in the *x*-direction, downgoing plate rotations occur in the free-subduction model (Model A), where the continental plate is dragged toward the oceanic subduction. Because the slab breaks off in all the models A to C, similar downgoing plate rotations occur, although forced convergence increases the component parallel to the convergence (Model B), which eventually overcome the rotations when far-field forcing is largest (Model C). The upper plate's stress magnitude is consistent in the three models, varying in the propagation length, suggesting that the upper plate's deformation is less dependent on the choice of boundary conditions.

3.2.2. Strain Field and Shear Zones Formation

In Model A, along the stalled collisional margin where break-off occurred, the deformation is accommodated mostly along a shear zone departing at ~45° from the margin, where shearing and distal transpression occur (Figure 4d). The lateral propagation of the shear zone is diverted into the oceanic back arc, attaining a curved strike, allowing the lateral extrusion of a sizeable block toward the retreating margin, while compression along the upper plate margin is minor. This pattern remains stable under forced convergence (Model B and C), with compression along the deforming areas progressively increasing, but not propagating further (Figure 4e).

In the oceanic back arc, strain rates and strain axes indicate uniaxial compression along the convergent margin and uniaxial extension in the back arc center (Figures 4d and 4e) in all the Models presented. In the upper plate, the tensional axes increasingly rotate clockwise from the collision's upper plate to the oceanic back-arc. The transcurrent shear zone joins the extensional basin in a T-joint, that is, it ends off joining the basin. The effect of forced convergence (Models B and C) mostly affects the strain magnitude, not the pattern. When external forcing exceeds the net oceanic margin forces (Model C), strain rates in the upper plate interiors are on average reduced. Most of the deformation is increasingly accommodated within the indented triangular area (Figure 4e).

3.2.3. Plate Thickness Variations

When subduction forces drive convergence (Model A), plate thickening occurs along the oceanic convergent margin at rates in excess of -2×10^{-15} s^{-1}, and it almost vanishes along the colliding margin, where the slab has broken off (Figures 4g and 7). Upper plate thinning rates values in excess of 2×10^{-15} s^{-1} are found in a narrow area in the back arc, which remains active throughout the whole simulation (Figure 9). Under forced convergence (Models B and C), this pattern remains essentially unperturbed, with hampered stretching in the back-arc when far-field forces overcome margin forces (Figure 4i).

In Model A, minor thickening occurs in the upper plate following break-off, localized at a distance from the indenting margin. Small negative values of -4×10^{-16} (Figures 4g and 7) are found at a distance up to

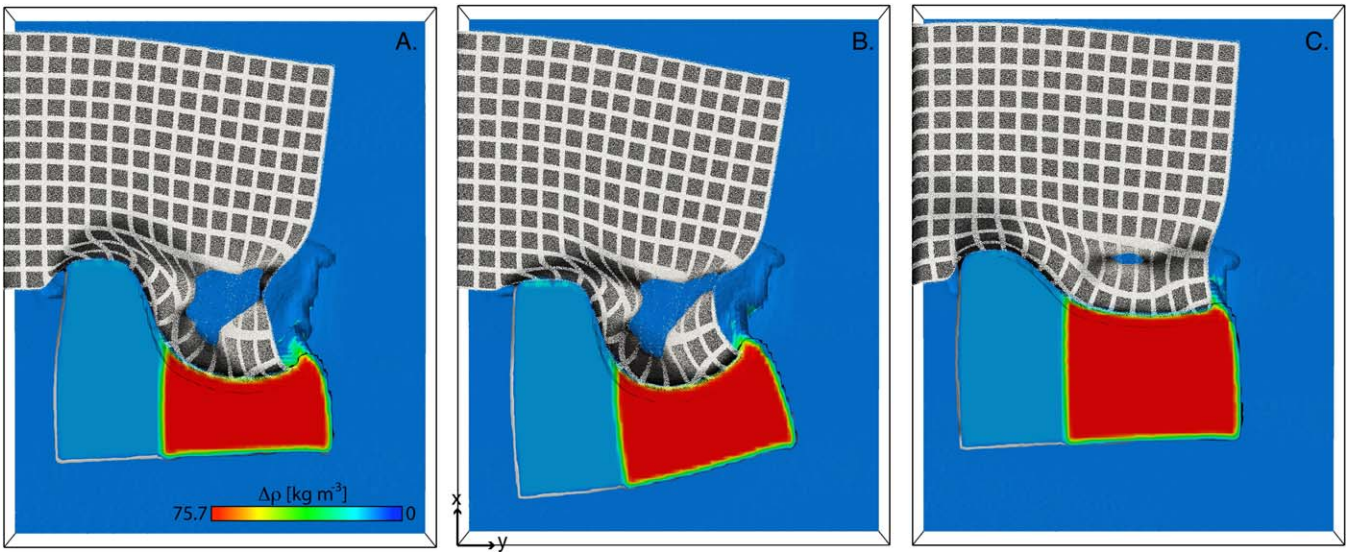

Figure 8. Final stage of the models and finite strain. Time of the final stage in Figure 3. Viscosity field contoured for $\eta_{eff}/\eta_0 = 10$. Density contrast plotted for upper mantle and downgoing plate. Lagrangian particles in the upper plate only, dark gray-black areas indicate areas of $\eta_{eff}/\eta_0 < 250$, color scale not shown. Finite strain assessments are by comparison with the initial stage of Figure 1.

200 km from the margin, bordering an area where no deformation occurs. Thickening here is associated with transpression, although no thickening is found along the shear zone closer to the margin, indicating a simple shearing regime. Small thickening occurs along the upper plate margin, suggesting that the lateral extrusion accommodates almost completely the convergence along the trench.

Forced convergence (Models B and C) induces broader thickening in the indented continental plate and at a distance, along the sheared zone. In Model B, the ridge push generates larger thickening rates of -4×10^{-16} close to the margin and -1.2×10^{-15} s^{-1} in the plate interiors along the shear zone (Figures 4h and 7). In Model C, far-field forcing drives larger thickening along the upper plate margin, with values of 1.7×10^{-15} s^{-1} (Figure 4i). In this model, the whole area comprised between the margin and the distant transpressional belt is under thickening, with larger rates in excess of 1.1×10^{-15} s^{-1} throughout.

The shearing belt at ~45° extends through the whole upper plate thickness and accommodates thickening in the plates interiors throughout the model evolution. In this sense, this represents an important rheological boundary.

3.2.4. Finite Strain

We compare in this section the finite strain in the models, after 800 km of oceanic subduction after the break-off occurred (Figure 8). The finite strain, illustrated by the model's particle grids, shows best the indentation and the lateral extrusion. In all models (A to C), large upper plate internal deformation localizes close to the collisional zone, where extrusion and/or thickening occur, and in the back-arc which is under extension. Three diverse long-term evolutions are observed, ranging from large lateral extrusion and no indentation following break-off in Model A (Figure 8a), to large indentation and negligible lateral extrusion, when the far-field forces are large (Figure 8c), Model C. In these models, the extrusion and indentation are measured as the displacement from the initial position.

In the subduction model undergoing break-off and no far-field forcing (Model A, Figure 8a), the oceanic margin migrates ~780 km trenchward, accommodating most of the 800 km convergence since break-off. Extreme thinning in the back arc leads to the formation of a spreading center, where mantle surfaces. Within the area in front of the colliding margin, progressive shearing result in varying offsets. The extrusion has a sinistral sense of shear, with offset increasing from the colliding margin towards the oceanic back arc. The horizontal offset is ~70 km along the 45° shear zone close to the colliding margin, and up to a maximum of ~230 km in the oceanic back arc. During the oceanic trench retreat, several blocks separate from the upper plate and migrate along with the margin, while undergoing rotation and stretching. The rotation follows the development of the margin curvature, with opposite spin sense on the sides of the trench,

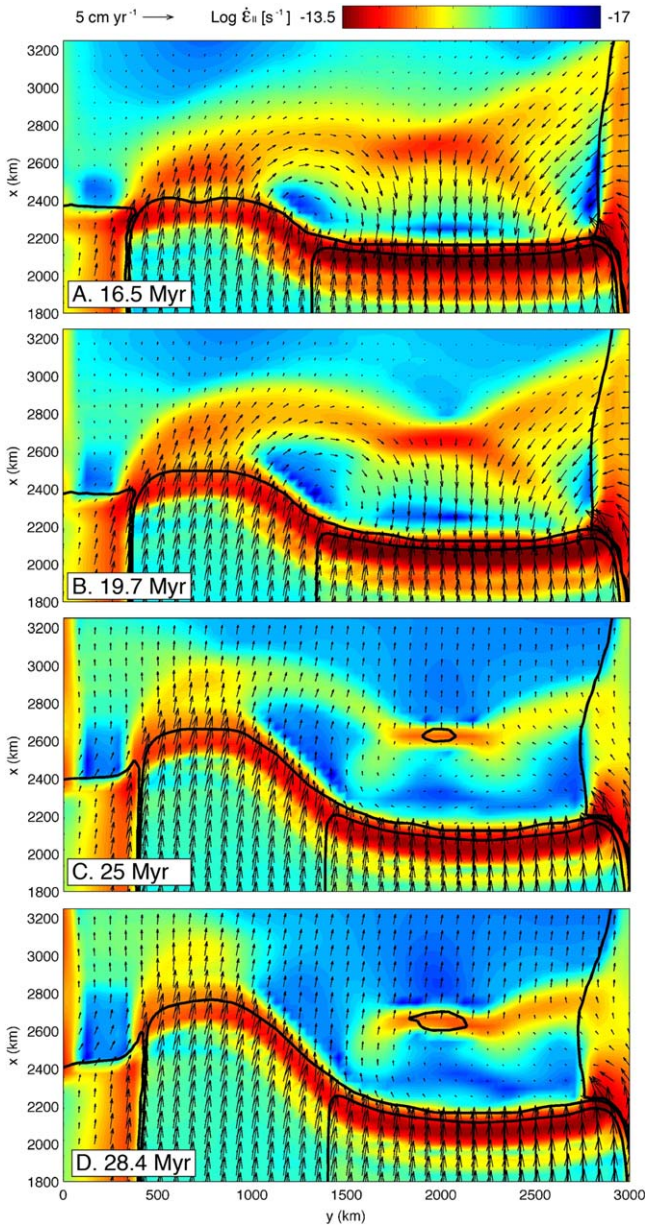

Figure 9. Time evolution of Model C with velocity vectors and second invariant of the strain rate tensor $\dot{\varepsilon}_{II}$. Black lines for viscosity contrasts $\eta_{eff}/\eta_0 = 10$, and for density contrast of 70 kg m^{-3}, indicating the oceanic lithosphere in the downgoing plate.

vanishing in the arc's center. The internal deformation of the blocks prevent rotation measurements; however, the largest rotation is ∼20° anticlockwise in the external side of the oceanic margin, and as large as ∼45° along the margin on the side of the continent.

In the model with ridge push forcing (Model B, Figure 8b), during the 800 km of convergence, similar back-arc extension occurs with trench migration of ∼700 km, however, indentation here is larger, ∼220 km. The horizontal offset is ∼70 km along the 45° shear zone close to the margin, increasing to a maximum of 200 km toward the oceanic back arc.

In the model where convergence is under far-field forcing (Model C), during the 800 km of convergence, the downgoing plate motions toward the trench eventually outpace the subduction rate, resulting in smaller trench retreat, a total of 350 km, half of the previous models (Figure 8c). The total indentation in this model is the same as the previous case ∼220 km, whereas continental subduction accommodates the remaining ∼580 km of convergence. The reduced oceanic margin retreat inhibits largely lateral extrusion, so that the largest offset measured along the sinistral shear zone is only ∼50 km, the smallest of the three cases. In front of the collisional margin lateral offset is almost negligible, however, as illustrated before, the deformation here is mostly accommodated by thickening, the most widespread in this model (Figure 4i).

3.3. Time-Scales of Extrusion Tectonics

In all the three models presented, extrusion is a transient response to the slab break-off perturbation. Coupling stresses increase in the upper plate interiors following the break-off and the redistribution and concentration of the slab mass [*Capitanio*, 2014], yet, these vanish as continental subduction along the stalled margin resumes.

In Figure 9, we show four steps of the model C (Figure 4c). The first step at 16.5 Myr, is ∼4 Myr after the break-off. At this stage, the weakening pattern is rather diffuse, although the strain rate magnitude is large, indicating that incipient collision is accommodated locally in front of the indenter. While stress coupling increases rapidly following break-off, extrusion lags due to rearrangement of the viscous slab and margin,

and the progressive formation of a stable shear zone across the upper plate (Figure 9a). Instead, in the oceanic back arc, deformation rates are already comparable to the largest measured in the model.

At 19.7 Myr, ~7 Myr after break-off, extrusion motions have increased and a shear pattern is established across the whole upper plate interior (Figure 9b). The deformation within the upper plate is mostly localized along the curved transcurrent shear zone. This sinistral strike-slip zone accompanies block lateral extrusion and joins to the oceanic back arc spreading center. The oceanic trench progressively migrates, while stretching localizes in an elongated back arc basin extending in a direction almost parallel to the margin. At this stage, the subducted continental lithosphere does not exceed ~200 km depth.

By 25 Myr, ~12 Myr after slab break-off, subduction along the stalled margin slowly resumes, and the extrusive motions fade. A total of 400 km of continental lithosphere has been subducted since break-off, thus reducing the slab buoyancy gradients along the margin. This results in the extrusion waning, and the relative growth of the far-field force signature (Figure 9c). At this stage, the coupling between the plates is partly sustained by the far-field forces, driving a net change in the upper plate velocity pattern, now with a larger convergence-parallel component, as the strain rate along the transcurrent shear zone decreases. It is important to note that the lithosphere does not recover its strength in the triangular area in front of the indenting margin, which continuously deforms. The transcurrent zone formed during extrusion now accommodates only compression. The depth of the subducted continental lithosphere in the mantle is 200–250 km.

By 28.4 Myr, that is 16 Myr after the break-off, extrusion has completely vanished, and the whole subduction upper plate system is controlled by far-field forcing (Figure 9d). The deformation pattern is similar to the previous step, although deformation rates are decreased, and lithospheric strength is partially recovered. The velocity pattern shows larger upper plate motions, indicating increased coupling. Along the oceanic subducting margin, the whole subduction zone is now migrating toward the upper plate, with away-from-trench motions throughout the upper plate. In this stage, the forces along the oceanic margin are almost in balance, and the oceanic margin advances slowly, as can be inferred from the small away-from-trench velocities. In the indented area, convergence is accommodated increasingly along the upper plate margin, while the plate interiors deformation wanes. At depth, the tip of the subducted lithosphere along this margin is found at 250–300 km.

By 35 Myr, 23 Myr after break-off, extrusion and indentation have completely faded in the upper plate interiors and deformation is accommodated along the margin. In this phase, the subducted slab tip has reached mid mantle depth, 350–380 km. During the following time, the continental slab extends to the transition zone establishing steady state subduction.

The duration of extrusion depends on the duration of the break-off perturbation, which vanishes as subduction resumes. In the model presented with continental buoyancy of -12.6 kg m^{-3} extrusion ceases within 23 Myr. When the negative buoyancy of the continent increases to -25.2 and -50.4 kg m^{-3}, the intraplate deformation vanishes by 16 and 11 Myr, respectively. All these models have the same evolution through the transient extrusion following break-off perturbation.

The partitioning of deformation into extrusion and thickening varies largely during the evolution. Extrusion is largest by 5–7 Myr after break-off has occurred, and progressively fades as subduction resumes. Instead, thickening and indentation, when sustained by far-field forces, evolve in the opposite way and are maximized in the initial stage, before the extrusion motions fully establish, and in the final stage, as extrusion fades. Because extrusion along weak shear zones is a less dissipative process than thickening, it accommodates most of the deformation when active.

4. Discussion

4.1. Models of Subduction and Break-Off

We have presented here models of subduction where break-off of the oceanic slab in front of the continent provides the driving mechanism for margin migrations and large-scale plate interior deformation. This illustrates that the coupling between upper plate, mantle and subduction has a relevant role for coupled trench evolution and upper plate tectonics.

The modeling of slab buoyancy variations along trenches during subduction has received some attention lately [*Capitanio*, 2014; *Duretz et al*., 2014; *Guillaume et al*., 2013; *Li et al*., 2013; *Magni et al*., 2014; *Moresi*

et al., 2014; *Sternai et al*., 2014]. Several models investigated the effect of buoyancy heterogeneities such as continent-ocean transitions along the subduction zone, similar to that addressed here. In all these models, the convergent margin is disrupted when continental lithosphere subducts, and retreat of the oceanic/denser slab with respect to the continental/buoyant one ensues. Several of these works have used nonlinear temperature-dependent and stress-dependent rheologies [*Duretz et al*., 2014; *Li et al*., 2013; *Magni et al*., 2014; *Sternai et al*., 2014], resulting in slab break-off during continent subduction. In all of these models lateral transport in the upper plate is found, with upper plate thickening and lateral motions largely enhanced by slab break-off, possibly accompanied by a curved shear zone [*Sternai et al*., 2014]. The outcomes of the published models are similar to that presented here, despite in our rheology the viscosity is linearly dependent on stress and independent of temperature.

It is important to note that the formation of curved shear zones is independent of the finite width of the plate, or model space boundary [*Capitanio*, 2014]. The curved shear zone follows the extrusion of a block of width linearly proportional to the downgoing plate stiffness, this is ∼1000 km for Earth like parameters [*Capitanio*, 2014]. Therefore, while the width of the subducting plate might affect the shape of the trench [e.g., *Bajolet et al*., 2013], it does not affect the plate interior deformation.

Notably, only the work of *Sternai et al*. [2014], shows the formation of a curve shear zone, similar to what found here. This shear zone accompanies the lateral extrusion of a rigid upper plate block toward the ongoing oceanic subduction margin. The main difference with the models presented here, is that in *Sternai et al*. [2014] a tear fault decouples the subducting oceanic and continental lithospheres along the trench, although no slab break-off occurs. However, these two mechanisms are similar in the sense that they increase the stress in the upper plate, driving faulting. A surge of stresses in the upper plate follows the continent collision under forced convergence, while here stress coupling is maximized by the complete break-off of the slab.

In the models of *Moresi et al*. [2014], the slab break-off drives transient lateral motions in the upper plate and strong margin deformation, similar to what is found here. In their models, upper plate rotations around a pole located approximately along the trench occur, with the formation of localized shearing accompanying the extrusion. Similar results where presented by *Regard et al*. [2005], who found that the partial slab break-off is cause for indentation of the upper plate and upper plate rotations.

Some of the published models have used imposed downgoing plate velocity to test the role of forced convergence. In the models of *Duretz et al*. [2014], *Li et al*. [2014], and *Sternai et al*. [2014], a range of velocity boundary conditions to the downgoing plate are imposed, resulting in upper plate strain regimes including lateral motions and compression above the slab break-off.

These models illustrate similar mechanisms, supporting the idea that the subduction process has a fundamental role in the evolution of plate margins and interiors. *Sternai et al*. [2014], originally highlighted the role of the mantle tractions during the subduction of heterogeneous plates in driving the extrusion motions and formation of a curved shear zone. Here, we confirm the role of mantle tractions, but additionally show that large-scale rotations, not coupled to the mantle [*Capitanio*, 2014], are driven by the combined indentation-retreat motions of a large subducting plate undergoing partial slab break-off. The combination of oceanic retreat and mantle flow coupling and indentation stresses are two mechanisms that act together, yet related to the same large-scale subduction dynamics.

4.2. Comparison With Models of Indentation and Extrusion

The deformation of the Asian continent as a result of collision and indentation of the Indian plate is a long-standing issue of plate tectonics. The indentation stresses have been invoked to explain the large-scale faulting pattern and the lateral extrusion in Asia [*Tapponnier and Molnar*, 1976; *Tapponnier et al*., 1982] or the thickening in front of the Indian indenter, when vertical thickening is accounted for [*England and McKenzie*, 1982; *Royden et al*., 1997]. Here we propose that continental deformation is best understood in the context of large-scale subduction-related processes. This model requires a more realistic assumption to explain the Asian tectonics and its evolution through time.

According to the classical indentation model, the lateral extrusion occurs by indentation of the upper plate with a stress-free boundary condition to the east [e.g., *Peltzer and Tapponnier*, 1988; *Schueller and Davy*, 2008; *Tapponnier et al*., 1982]. This represents an unconstrained side of the plate where the confining

stresses vanish and motions are free. This is arguably not the case on Earth, where the southeastern and eastern Asian plate margins are site of ongoing oceanic subduction, thus likely associated with large stresses, instead. Here, we have shown that the oceanic subducting margin should not be regarded as a "free side" but instead provides a fundamental, driving mechanism [*Sternai et al*., 2014].

The subducting margin of a wide heterogeneous plate (hosting oceanic and continental lithosphere) deforms upon continent subduction and slab break-off, controlling at the same time the indenting and retreating motions along the trench, and rotation and escape in the plate interiors (Figure 4). This introduces an asymmetry in the upper plate deformation and the shear zone propagates laterally. This initiates at the far corner of the indenter, and propagates towards the oceanic margin, where the shear zone is diverted into the oceanic back arc, attaining a curved strike (Figure 4). The shearing/faulting geometry and extrusion pattern in the models are similar to what predicted by the plastic slip line theory, generated by the 2-D indentation [*Molnar and Tapponnier*, 1975; *Tapponnier and Molnar*, 1976], however, this pattern is here explained as the effect of large-scale subduction. Furthermore, our model does not need to invoke preexisting heterogeneities in the Asian lithosphere, such as the Tarim basin, which has commonly invoked to favor the formation of large-scale strike slip faulting [*Cook and Royden*, 2008; *England and Houseman*, 1985], and instead explains the emergence of curved lithospheric-scale strike-slip faulting in homogeneous upper plates.

Our model predicts the occurrence of extrusion and stretching in the upper plate above the oceanic trench, providing an explanation for the enigmatic relation between the Red River Fault and the South China Sea opening in Southeast Asia. Here, the intersection of the Red River Fault with the South China Sea, the large-scale stretching and the paleomagnetic record in Borneo are at odd with the "free side" geometry of the indentation model [*Hall*, 2002; *Hall et al*., 2008], where strike-slip faults, such as the Red River Fault, should instead extend to the convergent margin. Our model predicts the overlap of the lateral escape with the back-arc stretching above a retreating oceanic slab, showing that the strike-slip fault must end into the extensional basin with a T joint, then obliterated as the basin grows, which is in agreement with the geological evidence [*Mazur et al*., 2012].

We showed that far-field forces are required to induce significant thickening in front of the indenter (Figures 4h and 4i). The localization of thickening is similar to what predicted by plane stress 2-D indentation models [e.g., *Cook and Royden*, 2008; *England and Houseman*, 1985; *England and McKenzie*, 1982; *Lechman et al*., 2011], however, the large-scale subduction-controlled 45° shear zone defines a rheological boundary in the upper plate (Figure 4), accommodating long-term thickening, and limiting further northward deformation migration, resulting in a bath-tub like thickening. This model is in agreement with what is observed in Tibet, where major deformation is limited by the Altyn Tagh fault at 45° with the colliding margin [e.g., *Tapponnier and Molnar*, 1976] and the Qilian Shan [*Yuan et al*., 2013] and throughout the Tibetan Plateau buildup history [*Liu-Zeng et al*., 2008]. This implies that the shear zones must be weaker than the surrounding lithosphere, and able to deform under stresses otherwise supported by stronger surrounding lithosphere. Such rheological boundaries are unlikely shallow features, but must be rather weak structures throughout the lithosphere, as inferred by means of tomography for the present-day Altyn Tagh [*Wittlinger et al*., 1998].

4.3. Insights on the Coupled Asian Continental Tectonics and Tethys Subduction Evolution

In this section, we discuss the insights the modeling offers into the large-scale Asian tectonics evolution during the Tethys closure (Figure 10).

We found that the necessary condition for margin migrations, indentation, extrusion, and back-arc stretching is the break-off along the colliding margin of a wide heterogeneous subducting plate (Figure 4). The subduction of the oceanic part alone can drive convergence of the large rigid continental plate, which is locally accommodated by indentation of the upper plate after the slab breaks off at the OCB (Figure 2). The models predicts the increased coupling after the slab break-off and the localization of strain along a belt ~45° from the trench, providing the conditions for reactivation of the Asian sutures and, more in general, compression in the Asian interiors. We have shown that transient large-scale extrusion follows partial slab break-off, whereas thickening and large indentation results from far-field forcing. The combination leads to strongly time-dependent continental tectonics.

Beneath the present-day position of India, remnants of the Tethys slab are found as positive tomographic anomalies at depth greater than 1000 km [*Hafkenscheid et al*., 2006; *Replumaz et al*., 2010b; *Van der Voo*

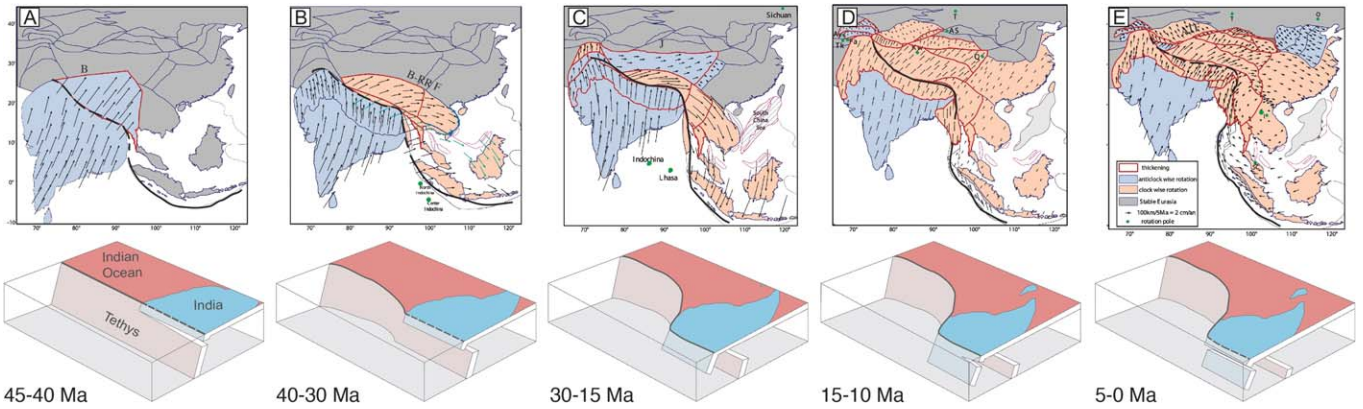

Figure 10. Reconstruction of Cenozoic Asian tectonics and velocity and Tethys and India subduction, in the Asia-fix reference frame. Redrawn from *Replumaz and Tapponnier* [2003], and *Replumaz et al*. [2014]. (top) Reconstructed velocity field for time intervals 45–40 Ma (a), 40–30 Ma (b), 30–15 Ma (c), 15–10 Ma (d), 5–0 Ma (e). Blue for anticlockwise rotations, pink for clockwise rotations, red contour for areas under thickening. Green larger circles rotation poles of clockwise rotations. Solid black thick line is the subducting margin, dashed lines for slab break-off episodes along the margin. (bottom) Reconstructions of the subduction in the upper mantle of the Tethys and Indian Ocean (in red) and Indian continental lithosphere (in blue). (b) Bangong Suture, B-RR F Bangong-Red River Fault, J Jinsha Suture, ATF Altyn Tagh Fault.

et al., 1999], with deep geometry suggesting a rather stationary margin during the closure of the oceanic basin. The Tethys slab detached at ∼45 Ma, and the Greater Indian continental lithosphere initiated subduction in the mantle shortly after [*Negredo et al*., 2007]. At that time, extrusion tectonics activated, with localized shearing within the upper plate [*Replumaz and Tapponnier*, 2003; *van Hinsbergen et al*., 2011a; *Yin*, 2010] (Figure 10a).

The reconstruction of the displacement field along these faults shows large-scale block rotation of the Southeast Asian block [*Leloup et al*., 2001], around a reconstructed pole located in the proximity of the trench, close to the location of the India-Tethys lithospheric boundary within the plate [*Replumaz and Tapponnier*, 2003] (green circles, Figure 10). The Asian blocks lateral extrusion likely accommodates most of the deformation in this time, prior to the broadening of the Tibetan plateau [*Tapponnier et al*., 2001]. Along the Southeast Asian margin, such extrusion is accompanied by stretching in the upper plate, where subsidence on thinned continental lithosphere started likely by 40 Ma [e.g., *Hall*, 2002; *Whittaker et al*., 2007 and references Therein] (Figure 10b) and lasted through the South China Sea opening, 32–16 Ma [*Briais et al*., 1993] (Figure 10c).

The large-scale margin evolution related to a single, wide plate includes the advance along the colliding margin and the retreat of the oceanic subducting trench, thus explaining the coupled Indian indentation and the inception of the Southeast Asian margin retreat with respect to stable Eurasia (Figure 8). This models predicts the increased coupling after the slab break-off and the localization of strain along a belt ∼45° from the trench, suggesting that partial slab break-off along the Indian margin during the large-scale Tethys plate subduction provided the conditions for reactivation of the Asian sutures and, more in general, compression in the Asian interiors.

The location of the large-scale reconstructed rotations pole in the ∼40–15 Ma time is in good agreement with the models A and B predicted poles (Figures 10b and 10c). Also, the inferred smaller thickening in Tibet in the early collision time [*Tapponnier et al*., 2001] is best in agreement with model A (slab buoyancy forces only), which allows us to infer that in this time far-field forces did not contribute much to the Asian tectonics. After this time, the Indian margin started its steady northward advance. Thickening in Tibet began as the Indian convergent margin advanced north, overriding the deeper sinking oceanic Tethys slab, and since then steadily migrated northward [*Guillot et al*., 2003; *Yin*, 2010]. Such margin migration can only be explained by growing external forces, which in our models are strictly needed to drive stable indentation (Models B and C).

The balance of deformation partitioning into extrusion and compression in Asia shows the progressive fading of the extrusion (rotation) motions, while compression increases and propagates to the upper plate interiors between ∼45 and ∼15 Ma [*Replumaz and Tapponnier*, 2003]. In our models, this balance is a consequence of resumed subduction along the continental collision margin, following the break-off. The

modeled sinking of the slab is in good agreement with the reconstructed depth of slab during this time deduced from tomographic positive anomalies [*Replumaz et al*., 2014], indicating that resumed subduction had reached mid-mantle depth (Figure 10c). As the subduction of Indian lithosphere fully developed to reach the transition zone, widespread compression propagated in the Asian continent interiors, and lateral extrusion completely vanished (Figure 10d). Our models provide an explanation for the vanishing extrusion as the consequence of the reestablished subduction along the collisional margin and the compression propagation as the effect of far-field forces.

Further constraints on the force balance behind Asian tectonics can be gained by the episodic Southeast Asian margin migration and the transient South China Sea spreading, occurring between 32 and 16 Ma [*Briais et al*., 1993] (Figure 10c). By the end of this stage, the trench retreat faded and became stationary ~15 Ma [*Whittaker et al*., 2007]. According the mechanisms highlighted by model C, where back-arc extension eventually vanishes, the end of the opening stage by ~15 Ma can be regarded as the consequence of the growth of the far-field forces with respect to the subduction force. Furthermore, in the models this condition induces widespread upper plate away-from-trench motions, with larger rates in the indented plate with respect to the oceanic back arc. This pattern best fits the reconstructed motions within the Asian continent around 15–10 Ma (Figure 10d), with large-scale away-from-trench motions inferred by shortening, in central Asia larger than in eastern Asia [*Replumaz and Tapponnier*, 2003]. This regime is also indicative of slip vanishing along the Red River Fault [*Leloup et al*., 2001] and a general demise of Asian strike-slip motions [*Replumaz and Tapponnier*, 2003; *van Hinsbergen et al*., 2011a; *Yin*, 2010] as in the models.

The tectonic evolution in the last 10–5 Ma is characterized by renewed strike slip motions, such as along the Altyn Tagh fault, with minor compression, extension in Tibet and rather constant rotations since the Miocene [*Replumaz and Tapponnier*, 2003; *van Hinsbergen et al*., 2011a; *Yin*, 2010] (Figure 10e). The renewed rotations can be explained by the completion of the second episode of slab break-off, reconstructed beneath the Indian margin between 25 and 15 Ma [*Li et al*., 2008; *Replumaz et al*., 2010a]. This episode removed the Indian subducting lithosphere, and subsequently subduction resumed beneath Tibet, and it is currently imaged at depth of ~400 km. Although this subduction stage is similar to that reconstructed between 30 and 15 Ma (Figure 10c), the further propagation of compression in the plate can be explained, as in the previous stage, by the effect of large far-field forces. To support this inference, the location of the renewed rotation pole of the Indochina and South China blocks has migrated further in the upper plate. The location as well as the migration of the rotation poles is remarkably similar to the position and migration due to the effect of large far-field forces during slab break-off showed in Figure 4.

Some features of this area are not captured by our models. For instance, the curved shape of the Himalayan front and of the Indian lithosphere at depth might be possibly related to other processes not modeled here. In *Capitanio and Replumaz* [2013], we have proposed that the Western Syntaxis with long-term underplating might be a consequence of the slab break-off and resumed subduction. Alternatively, it has been proposed that the curvature might develop as a result of the upper plate rheology [*Bajolet et al*., 2013]. Another cause could be the development of a tear in the slab beneath the Eastern Syntaxis [*Li et al*., 2008], as the tearing in the slab allows for tighter trench curvatures [*Capitanio*, 2014; *Sternai et al*., 2014]. However, these are likely second-order features, and do not affect the understanding provided here.

5. Conclusions

In this paper, we investigate on the role that the Indian continents subduction and slab break-off during the Tethys oceanic closure had on the tectonics of the Asian continent interior by means of three-dimensional numerical models. We systematically model subduction force perturbations due to continental lithosphere entrainment and slab break-off, in relation with external forcing, such as ridge push and far-field forces, and focus on the plate margin and interior large-scale tectonics.

As the lithospheric slab breaks off along the colliding margin, the convergent margin is disrupted, with retreat of the oceanic subduction trench and back arc stretching, and large-scale extrusion and rotations from colliding toward the oceanic margin. Forces external to the subduction, such as ridge push and far-field forces, when larger than margin forces, drive indentation along the colliding margin and thickening in the upper plate. When the far-field force further increases above the ridge push, the retreat of the oceanic trench is hampered, which has a dramatic effect on the upper plate tectonics, as it prevents lateral extrusion

and favors thickening. Based on the relative role of margin and external forces, we show three large-scale strain regimes in the upper plate interiors: mostly extrusion, extrusion and thickening along the collisional margin and thickening only. These regimes emerge when no far-field forces, ridge push, and a force approximately twice the ridge push, respectively, alter the subduction force balance. Therefore, the large-scale subduction process, where collisional and oceanic retreating margins and upper plate interiors are intimately connected, has a fundamental control on the evolution and strong asymmetry of upper plate interiors tectonics. In particular, we found that balance between the slab break-off-driven buoyancy perturbation and the far-field forces controls the partitioning between extrusion, indentation and back-arc tectonics.

When compared to the Cenozoic Asian tectonics, the balance between subduction dynamics undergoing slab break-off perturbations and the external forces provides an explanation for the time-dependent Asian tectonics, where the extrusion, with continent-scale block rotations, lasted between ∼45 and ∼20 Ma, faded leaving the whole Asian plate under compression, and then was renewed ∼10 Ma. The comparison with the model supports the idea that slab break-off episodes and the relative growth of far-field forces are likely drivers of the Indian indentation and Southeast Asian margin episodic retreat. Most importantly, the models provide viable mechanisms for the asymmetric and time-dependent lithospheric thickening and large-scale faulting in Asia, without invoking unrealistic stress-free boundaries, nor preexisting Asian continent heterogeneities.

Concluding, when compared to existing models of Asian tectonics, the coupled subduction dynamics-upper plate model presented here requires no assumptions on the upper plate nature, such as preexisting heterogeneities or rigid blocks, nor on its rheological variations. By Occam's razor, this model should be preferred.

Acknowledgments
This paper benefited from the comments of P. Sternai, F. Crameri, and an anonymous reviewer. This work was supported by the *Australian Research Council*'s Project DE130100604 and by the *NCI National Facility* systems at the Australian National University through the *National Computational Merit Allocation Scheme*, supported by the Australian Government, and by a grant from Labex OSUG@2020 (Investissements d'avenir – ANR10 LABX56) and the ANR DSP-Tibet. F.A.C. acknowledges discussions with P. Tapponnier and G. Houseman.

References

Bajolet, F., A. Replumaz, and R. Lainé (2013), Orocline and syntaxes formation during subduction and collision, *Tectonics*, *32*, 1529–1546, doi:1510.1002/tect.20087.
Becker, T. W., and C. Faccenna (2011), Mantle conveyor beneath the Tethyan collisional belt, *Earth Planet Sci. Lett.*, *310*, 453–461.
Becker, T. W., and R. J. O'Connell (2001), Predicting plate velocities with mantle circulation models, *Geochem. Geophys. Geosyst.*, *2*, 1601.
Bercovici, D. (1995), On the purpose of toroidal motions in a convecting mantle, *Geophys. Res. Lett.*, *22*, 3107–3110.
Billen, M., and G. Hirt (2005), Newtonian versus non-Newtonian upper mantle viscosity: Implications for subduction initiation, *Gephys. Res. Lett.*, *32*, L19304, doi:10.1029/2005GL023457.
Briais, A., P. Patriat, and P. Tapponnier (1993), Updated interpretation of magnetic-anomalies and sea-floor spreading stages in the South China Sea: Implications for the Tertiary tectonics of South-Asia, *J. Geophys. Res.*, *98*, 6299–6328.
Burkett, E. R., and M. I. Billen (2010), Three-dimensionality of slab detachment due to ridge–trench collision: Llaterally simultaneous boudinage versus tear propagation, *Geochem. Geophys. Geosyst.*, *11*, Q11012, doi:10.1029/2010GC003286.
Burov, E. (2007), Plate rheology and mechanics, in *Treatise of Geophysics*, edited by A. B. Watts, pp. 99–151, Elsevier, Amsterdam.
Cande, S. C., and D. R. Stegman (2011), Indian and African plate motions driven by the push force of the Réunion plume head, *Nature*, *475*, 47–52.
Capitanio, F. A. (2014), The dynamics of extrusion tectonics: Insights from numerical modeling, *Tectonics*, *33*, 2361–2381, doi:2310.1002/2014TC003688.
Capitanio, F. A., and A. Replumaz (2013), Subduction and slab breakoff controls on Asian indentation tectonics and Himalayan western syntaxis formation, *Geochem. Geophys. Geosyst.*, *14*, 3515–3531, doi: 10.1002/ggge.20171.
Capitanio, F. A., G. Morra, S. Goes, R. F. Weinberg, and L. Moresi (2010a), India–Asia convergence driven by the subduction of the Greater Indian continent, *Nat. Geosci.*, *3*(2), 136–139.
Capitanio, F. A., D. R. Stegman, L. Moresi, and W. Sharples (2010b), Upper plate controls on deep subduction, trench migrations and deformations at convergent margins, *Tectonophysics*, *483*, 80–92.
Capitanio, F. A., C. Faccenna, S. Zlotnik, and D. R. Stegman (2011), Subduction dynamics and the origin of Andean orogeny and Bolivian Orocline, *Nature*, *480*, 83–86.
Clark, M. K. (2012), Continental collision slowing due to viscous mantle lithosphere rather than topography, *Nature*, *483*, 74–77.
Cloos, M. (1993), Lithospheric buoyancy and collisional orogenesis: Subduction of oceanic plateaus, continental margins, island arcs, spreading ridges, and seamounts, *Geol. Soc. Am. Bull.*, *105*, 715–737.
Conrad, C. P., and C. Lithgow-Bertelloni (2002), How mantle slabs drive plate tectonics, *Science*, *298*(5591), 207–209.
Cook, K. L., and L. H. Royden (2008), The role of crustal strength variations in shaping orogenic plateaus, with application to Tibet, *J. Geophys. Res.*, *113*, B08407, doi:10.1029/2007JB005457.
Copley, A., J. P. Avouac, and J.-Y. Royer (2010), India-Asia collision and the Cenozoic slowdown of the Indian plate: Implications for the forces driving plate motions, *J. Geophys. Res.*, *115*, B03410, doi:10.1029/2009JB006634.
Crameri, F., P. Tackley, I. Meilick, T. Gerya, and B. Kaus (2012), A free plate surface and weak oceanic crust produce single-sided subduction on Earth, *Geophys. Res. Lett.*, *39*, L03306, doi:10.01029/02011GL050046.
Duretz, T., S. M. Schmalholz, and T. V. Gerya (2012), Dynamics of slab detachment, *Geochem. Geophys. Geosyst.*, *13*, Q03020,doi:10.1029/2011GC004024.
Duretz, T., T. V. Gerya, and W. Spakman (2014), Slab detachment in laterally varying subduction zones: 3-D numerical modeling, *Geophys. Res. Lett.*, *41*, 1951–1956, doi:1910.1002/2014GL059472.
England, P., and D. McKenzie (1982), A thin viscous sheet model for continental deformation, *Geophys. J. R. Astron. Soc.*, *70*, 295–321.

England, P., and P. Molnar (1997), Active deformation of Asia: From kinematics to dynamics, *Science*, *278*(5338), 647–650.
England, P., G. Houseman, and L. Sonder (1985), Length scales for continental deformation in convergent, divergent, and strike-slip environments: Analytical and approximate solutions for a thin viscous sheet model, *J. Geophys. Res.*, *90*, 3551–3557.
Flesch, L. M., A. J. Haines, and W. E. Holt (2001), Dynamics of the India-Eurasia collision zone, *J. Geophys. Res.*, *106*, 16,435–16,460.
Funiciello, F., C. Faccenna, and D. Giardini (2004), Role of lateral mantle flow in the evolution of subduction systems: Insights from laboratory experiments, *Geophy. J. Int.*, *157*, 1393–1406.
Gerya, T. V., D. A. Yuen, and W. V. Maresch (2004), Thermomechanical modeling of slab detachment, *Earth Planet Sci. Lett.*, *226*, 101–116.
Ghosh, A., and W. Holt (2012), Plate motions and stresses from global dynamic models, *Science*, *335*, 838–843.
Ghosh, A., W. E. Holt, L. M. Flesch, and A. J. Haines (2006), Gravitational potential energy of the Tibetan Plateau and the forces driving the Indian plate, *Geology*, *34*(5), 321–324.
Goes, S., F. A. Capitanio, G. Morra, M. Seton, and D. Giardini (2011), Signatures of downgoing plate-buoyancy driven subduction in Cenozoic plate motions, *Phys. Earth Planet Int.*, *184*(1-2), 1–13.
Guillaume, B., L. Husson, F. Funiciello, and C. Faccenna (2013), The dynamics of laterally variable subductions: Laboratory models applied to the Hellenides, *Solid Earth*, *5*, 315–363.
Guillot, S., E. Garzanti, D. Baratoux, D. Marquer, G. Mahéo, and J. de Sigoyer (2003), Reconstructing the total shortening history of the NW Himalaya, *Geochem. Geophys. Geosyst.*, *4*(7), 1064, doi:10.1029/2002GC000484.
Gurnis, M., C. Eloy, and S. Zhong (1997), Free-surface formulation of mantle convection—II. Implication for subduction-zone observables, *Geophy. J. Int.*, *127*(3), 719–727.
Hafkenscheid, E., M. J. R. Wortel, and W. Spakman (2006), Subduction history of the Tethyan region derived from seismic tomography and tectonic reconstructions, *J. Geophys. Res.*, *111*, BO8401, doi:10.1029/2005JB003791.
Hall, R. (2002), Cenozoic geological and plate tectonic evolution of SE Asia and the SW Pacific: Computer-based reconstructions, model and animations, *J. Asian Earth Sci.*, *20*(4), 353–431.
Hall, R., M. van Hattum, and W. Spakman (2008), Impact of India–Asia collision on SE Asia: The record in Borneo, *Tectonophysics*, *451*, 366–389.
Houseman, G., and P. England (1993), Crustal thickening versus lateral expulsion in the Indian-Asian continental collision, *J. Geophys. Res.*, *98*, 12,233–12,249.
Iaffaldano, G., L. Husson, and H. P. Bunge (2011), Monsoon speeds up Indian plate motion, *Earth Planet Sci. Lett.*, *304*, 503–510.
Jadamec, M. A., and M. Billen (2010), Reconciling surface plate motions with rapid three-dimensional mantle flow around a slab edge, *Nature*, *465*(7296), 338–341.
Karato, S., and P. Wu (1993), Rheology of the upper mantle: A synthesis, *Science*, *260*, 771–778.
Kohlstedt, D. L., B. Evans, and S. J. Mackwell (1995), Strength of the lithosphere: Constraints imposed by laboratoy experiments, *J. Geophys. Res.*, *100*, 17,587–17,602.
Lechman, S. M., D. A. May, B. J. P. Kaus, and S. M. Schmalholz (2011), Comparing thin-sheet models with 3-D multilayer models for continental collision, *Geophys. J. Int.*, *187*, 10–33.
Leloup, P. H., N. Arnaud, R. Lacassin, J. R. Kienast, T. M. Harrison, T. T. P. Trong, A. Replumaz, and P. Tapponier (2001), New constraints on the structure, thermochronology, and timing of the Ailao Shan-Red River shear zone, SE Asia, *J. Geophys. Res.*, *106*, 6683–6732.
Li, C., R. D. van der Hilst, A. S. Meltzer, and E. R. Engdahl (2008), Subduction of the Indian lithosphere beneath the Tibetan Plateau and Burma, *Earth Planet Sci. Let.*, *274*, 157–168.
Li, Z. H., Z. Xu, T. V. Gerya, and J. P. Burg (2013), Collision of continental corner from 3-D numerical modeling, *Earth Planet Sci. Lett.*, *380*, 98–111.
Liu-Zeng, J., P. Tapponnier, Y. Gaudemer, and L. Ding (2008), Quantifying landscape differences across the Tibetan plateau: Implications for topographic relief evolution, *J. Geophys. Res.*, *113*, F04018, doi:04010.01029/02007JF000897.
Magni, V., C. Faccenna, J. van Hunen, and F. Funiciello (2014), How collision triggers backarc extension: Insight into Mediterranean style of extension from 3-D numerical models, *Geology*, *42*(6), 511–514.
Mattauer, M., P. Matte, and J. L. Olivet (1999), A 3D model of the India-Asia collision at plate scale, *C. R. Acad. Sci.*, *328*(8), 499–508.
Mazur, S., C. Green, M. Stewart, J. Whittaker, S. Williams, and S. Bouatmani (2012), Displacement along the Red River fault constrained by extension estimates and plate reconstructions, *Tectonics*, *31*, TC5008, doi:5010.1029/2012TC003174.
Molnar, P. (1988), Continental tectonics in the aftermath of plate tectonics, *Nature*, *335*, 131–137.
Molnar, P., and H. Lyon-Caen (1988), Some simple physical aspect of the support, structure, and evolution of mountain belts, *Geol. Soc. Am. Spec. Pap.*, *218*, 179–207.
Molnar, P., and P. Tapponnier (1975), Cenozoic tectonics of Asia: Effects of a continental collision, *Science*, *189*(4201), 419–426.
Moresi, L., P. G. Betts, M. S. Miller, and R. A. Cayley (2014), Dynamics of continental accretion, *Nature*, *508*, 245–248, doi:10.1038/nature13033.
Moresi, L., F. Dufour, and H. B. Mülhaus (2003), A lagrangian integration point finite element method for large deformation modeling of viscoelastic geomaterials, *J. Comput. Phys.*, *184*, 476–497.
Morra, G., K. Regenauer-Lieb, and D. Giardini (2006), On the curvature of oceanic arcs, *Geology*, *34*(10), 877–880.
Negredo, A. M., A. Replumaz, A. Villaseñor, and S. Guillot (2007), Modeling the evolution of continental subduction processes in the Pamir–Hindu Kush region, *Earth Planet Sci. Lett.*, *259*, 212–225.
Paulson, A., S. Zhong, and J. Wahr (2007), Inference of mantle viscosity from GRACE and relative sea level data, *Geophys. J. Int.*, *171*, 497–508.
Peltzer, G., and P. Tapponnier (1988), Formation and evolution of strike-slip faults, rifts, and basins during the India-Asia collision: An experimental approach, *J. Geophys. Res.*, *93*, 15,085–15,117.
Regard, V., C. Faccenna, J. Martinod, and B. O. Slab (2005), Pull and indentation tectonics: insights from 3D laboratory experiments, *Phys. Earth Plan. Int.*, *149*, 99–113.
Replumaz, A., and P. Tapponnier (2003), Reconstruction of the deformed collision zone Between India and Asia by backward motion of lithospheric blocks, *J. Geophys. Res.*, *108*(B6), 2285, doi:10.1029/2001JB000661.
Replumaz, A., H. Kárason, R. D. van der Hilst, J. Besse, and P. Tapponnier (2004), 4-D evolution of SE Asia's mantle from geological reconstructions and seismic tomography, *Earth Planet Sci. Lett.*, *221*, 103–115.
Replumaz, A., A. M. Negredo, S. Guillot, and A. Villaseñor (2010a), Multiple episodes of continental subduction during India/Asia convergence: Insight from seismic tomography and tectonic reconstruction, *Tectonophysics*, *483*, 125–134.
Replumaz, A., A. M. Negredo, A. Villaseñor, and S. Guillot (2010b), Indian continental subduction and slab break-off during Tertiary collision, *Terra Nova*, *22*, 290–296.

Replumaz, A., F. A. Capitanio, S. Guillot, A. M. Negredo, and A. Villaseñor (2014), The coupling of Indian subduction and Asian continental tectonics, *Gondwana Res.*, *26*, 608–626.
Royden, L. H., B. C. Burchfiel, R. W. King, E. Wang, Z. Chen, F. Shen, and Y. Liu (1997), Surface deformation and lower crustal flow in Eastern Tibet, *Science*, *276*, doi:10.1126/science.1276.5313.1788.
Schellart, W. P., and L. Moresi (2013), A new driving mechanism for backarc extension and backarc shortening through slab sinking induced toroidal and poloidal mantle flow: Results from dynamic subduction models with an overriding plate, *J. Geophys. Res. Solid Earth*, *118*, 3221–3248, doi:10.1002/jgrb.50173.
Schueller, S., and P. Davy (2008), Gravity influenced brittle-ductile deformation and growth faulting in the lithosphere during collision: Results from laboratory experiments, *J. Geophys. Res.*, *113*, B12404, doi:10.1029/2007JB005560.
Stegman, D. R., J. Freeman, W. P. Schellart, L. Moresi, and D. May (2006), Influence of trench width on subduction hinge retreat rates in 3-D models of slab rollback, *Geochem. Geophys. Geosyst.*, *7*(3), 1–22.
Sternai, P., L. Jolivet, A. Menant, and T. V. Gerya (2014), Driving the upper plate surface deformation by slab rollback and mantle flow, *Earth Planet Sci. Lett.*, *405*, 110–118.
Tapponnier, P., and P. Molnar (1976), Slip-line field theory and large-scale continental tectonics, *Nature*, *264*, 319–324.
Tapponnier, P., G. Peltzer, A. Y. Le Dain, R. Armijo, and P. Cobbold (1982), Propagating extrusion tectonics in Asia: New insights from simple experiments with plasticine, *Geology*, *10*, 611–616.
Tapponnier, P., X. Zhiqin, F. Roger, B. Meyer, N. Arnaud, G. Wittlinger, and Y. Jinsui (2001), Oblique stepwise rise and growth of the Tibet Plateau, *Science*, *294*, 1671–1677.
Turcotte, D. L., and G. Schubert (1982), *Geodynamics, Application of Continuum Mechanics to Geological Problems*, John Wiley, N. Y.
Van der Voo, R., W. Spakman, and H. Bijwaard (1999), Tethyan subducted slabs under India, *Earth Planet Sci. Lett.*, *171*, 7–20.
van Hinsbergen, D. J. J., P. Kapp, G. Dupont-Nivet, P. C. Lippert, P. G. DeCelles, and T. H. Torsvik (2011a), Restoration of Cenozoic deformation in Asia and the size of Greater India, *Tectonics*, *30*, TC5003, doi:10.1029/2011TC002908.
van Hinsbergen, D. J. J., B. Steinberger, P. V. Doubrovine, and R. Gassmöller (2011b), Acceleration and deceleration of India-Asia convergence since the Cretaceous: Roles of mantle plumes and continental collision, *J. Geophys. Res.*, *116*, B06101, doi:10.1029/2010JB008051.
van Hunen, J., and M. B. Allen (2011), Continental collision and slab break-off: A comparison of 3D numerical models with observations, *Earth Planet Sci. Lett.*, *302*, 27–37.
Whittaker, J. M., R. D. Müller, M. Sdrolias, and C. Heine (2007), Sunda-Java trench kinematics, slab window formation and overriding plate deformation since the Cretaceous, *Earth Planet Sci. Lett.*, *255*, 445–457.
Wittlinger, G., P. Tapponnier, G. Poupinet, J. Mei, S. Danian, G. Herquel, and F. Masson (1998), Tomographic evidence for localized lithospheric shear along the Altyn Tagh Fault, *Science*, *282*(5386), 74–76.
Yin, A. (2010), Cenozoic tectonic evolution of Asia: A preliminary synthesis, *Tectonophysics*, *488*, 293–325.
Yuan, D., et al. (2013), The growth of northeastern Tibet and its relevance to large-scale continental geodynamics: A review of recent studies, *Tectonics*, *32*, 1358–1370, doi:10.1002/tect.20081.
Zahirovic, S., R. D. Müller, M. Seton, N. Flament, M. Gurnis, and J. Whittaker (2012), Insights on the kinematics of the India-Eurasia collision from global geodynamic models, *Geochem. Geophys. Geosyst.*, *13*, Q04W11, doi:10.1029/2011GC003883.
Zhong, S., and M. Gurnis (1995), Mantle convection with plates and mobile, faulted plate margins, *Science*, *267*, 838–843.